

POLITECNICO DI TORINO

Corso di Laurea in Ingegneria Aerospaziale

Master Degree Thesis

**Design of Sliding Mode
Techniques for a CMG-based
Testbed Attitude Control System**



Academic Supervisors

Prof. Elisa Capello

Prof. Satoshi Satoh

Candidate

Antonio D'Ortona

April 2021

Abstract

The observation of the universe, the Earth monitoring, the docking of a capsule on the ISS, all these things require a certain attitude to carry out their tasks, so a robust attitude controller should be designed. The following thesis describes the design of a Sliding Mode Control (SMC) for a CMG (Control Moment Gyro) based testbed. A testbed is a platform for performing rigorous and replicable testing of scientific theories, new technologies, calculation tools and many control law is being developed on it. The testbed is driven by four CMGs which are torque generators used to perform attitude manoeuvre thanks to angular momentum conservation. The main reason to choose the Sliding mode control (SMC), which is a well-established method for control of nonlinear systems, is its robustness versus imprecise knowledge of the plant to control, because there will be always a discrepancy between the real plant and its mathematical model used for controller design. Two sliding mode techniques have been developed: a Super twisting and an adaptive continuous twisting. The second one has the ability to change its gains in real time to track controlled variables even if system parameters are unknown or if they change over time, this ability increases the robustness of the control system, since it is able to handle disturbances and adjust the gains.

In the second part of this thesis, a mathematical spacecraft model has been developed taking into account the effects deriving from appendages flexibility. The attitude maneuvering or the effect of external disturbances can produce continuous vibration of flexible appendages that interferes with the attitude control. The attitude dynamics of satellite considered is driven by the same CMGs actuators used on the testbed, while a cluster of thrusters manage the position dynamics by an H_∞ control law. In particular, the study is applied to a rendezvous manoeuvre, in which a moving satellite (Chaser) is trying to reach a second satellite (Target). In this case, a fixed Target is considered, furthermore both position and attitude dynamics is modeled for the Chaser including orbital disturbances.

Both scenarios are simulated by *Matlab* and *Simulink* software, in which the dynamics, guidance and control algorithms are implemented. Lastly, the testbed control algorithm has been converted in *C++* programming language and used to perform experiments on the testbed located at the Yamada's laboratory at Osaka University.

Contents

List of Figures	5
List of Tables	7
1 Introduction	9
1.1 Overview of the work	13
2 Attitude dynamics and CMG-based testbed	16
2.1 Reference frames	16
2.1.1 Inertial frame	16
2.1.2 Body reference frame	17
2.1.3 LVLH frame	18
2.1.4 The quaternions	18
2.2 Attitude dynamics	20
2.2.1 Euler's equation	20
2.2.2 CMG-based spacecraft dynamic equation	21
2.2.3 Gravity torque disturbance	24
2.2.4 Kinematic equation of motion	25
2.3 Simulation environment	25
3 Sliding Mode control (SMC)	29
3.1 Introduction to control theory	29
3.1.1 Introduction to SMC	30
3.1.2 Design of sliding mode control	32
3.2 Super-twisting SMC	34
3.3 Adaptive continuous Twisting (ACTW)	36
3.4 Simulation results	37
3.4.1 STW results	38
3.4.2 ACTW results	41
4 Attitude and position dynamics of a flexible spacecraft	49
4.1 Flexible spacecraft attitude model	50

4.1.1	Sub-bodies division and modal analysis	51
4.2	Position dynamics and control	53
4.2.1	Position actuator model	54
4.2.2	H_∞ position controller	55
4.3	Orbital manoeuvres	57
4.3.1	Hohmann transfer	58
4.3.2	Radial boost	58
4.4	Orbital disturbances	59
4.4.1	Aerodynamic drag	59
4.4.2	Gravity gradient	60
4.5	Simulation environment and results	61
5	Conclusions	70
A	Euler angles	73
B	Flexible dynamics	74
C	H_∞	76
C.1	L_\star norms	76

List of Figures

1.1	Testbed with 4 CMGs in pyramidal configuration	12
1.2	Experimental testbed that replicates the spacecraft attitude dynamics[8]	13
2.1	Earth Centered Frame [25]	17
2.2	Body Reference Frame in CMG cluster [8]	18
2.3	LVLH reference frame [36]	19
2.4	Euler's Theorem	19
2.5	Configuration of a pyramidal testbed equipped with 4 CMGs [33][18]	21
2.6	Gravity torque in the experimental setup [11]	24
2.7	Simulink scheme	26
3.1	Mass spring damper 1D model	29
3.2	Block diagram representation of a closed loop control system	30
3.3	Trajectory on the state plane	32
3.4	Phase plane trajectory of Super-twisting algorithm [40] (pp 156) . .	35
3.5	Vetorial part of quaternion (STW)	39
3.6	Angular velocity of testbed (STW)	39
3.7	Gimbal angles (STW)	40
3.8	Gimbal rates (STW)	40
3.9	Angular velocities steady-state error (STW)	41
3.10	Vetorial part of quaternion (ACTW)	42
3.11	Angular velocity of testbed (ACTW)	42
3.12	Gimbal angles (ACTW)	43
3.13	Gimbal rates (ACTW)	43
3.14	Angular velocities steady-state error (ACTW)	44
3.15	Vetorial part of quaternion (ACTW) when an higher disturbance is applied	44
3.16	Angular velocity of testbed (ACTW)when an higher disturbance is applied	45
3.17	Vetorial part of quaternion (STW) when an higher disturbance is applied	45

3.18 Angular velocity of testbed (STW) when an higher disturbance is applied	46
3.19 Gimbal rates (ACTW) when an higher disturbance is applied	46
3.20 Gimbal rates (STW) when an higher disturbance is applied	47
4.1 Discrete-parameter appendage sub-body coordinates	51
4.2 Spacecraft CAD model	52
4.3 Thruster scheme on the spacecraft [15]	54
4.4 System scheme	55
4.5 Bode diagram [38] (pp 11)	56
4.6 Hohmann transfer: inertial frame on the left, <i>LVLH</i> frame on the right [19](pp 38-52)	58
4.7 Transfer along V-bar by radial impulses [19] (pp 55).	59
4.8 Gravity gradient effect [5]	61
4.9 Simulink scheme	62
4.10 Vectorial part of quaternion	64
4.11 Variation of angular velocity of spacecraft	64
4.12 Time history of gain L	65
4.13 Time history of $\dot{\eta}$ contribution	65
4.14 Time history of $\ddot{\eta}$ contribution	66
4.15 Time history of η	66
4.16 Time history of gravity gradient disturbance	67
4.17 Rendezvous manoeuvre	67
4.18 Time history of chaser position	68
4.19 Force due to thrusters	68

List of Tables

2.1	Physical properties of the testbed	26
2.2	Input constraint	27
3.1	STW parameters	38
3.2	ACTW parameters	41
4.1	Physical properties of the spacecraft	62
4.2	Attitude Controller parameters	62

Chapter 1

Introduction

The attitude of a satellite in space is a fundamental aspect to reach the mission purposes: just consider all missions that require a proper payload pointing (camera or other scientific instruments), solar panel targeting, or performing a thermal control. The attitude and orbit control system (AOCS) is a complex system that allows to steer the attitude and position of a spacecraft. When talking about the AOCS, we refer to the set of two subsystems: Attitude determination and control system (ADCS) that provides stability, determines and controls the attitude through the use of sensors and actuators and the Orbit determination and control System, system concerning orbital motions, hence the trajectory of the spacecraft. These systems work in synergy to achieve the success of the mission which provide for rendezvous manoeuvre, docking¹ and proximity operations [20]. This thesis focuses on the attitude control that stabilises the spacecraft motion by removing disturbances and, depending on the mission, this system has to satisfy many requirements such as pointing accuracy, directional velocity (*slew*) and stability (*jitter*). Another key feature is robustness, which is the ability of closed loop system to be insensitive to changes in system parameters. In addition to this, simulations have to be performed in order to have a precise idea of the behaviour of the system and how to design the control law. However, the system mathematical model is often difficult to model due to the presence of non-linearities, which should be neglected variables or other simplifications, these models are not always reliable. Beside these motivations some dynamic phenomena could be neglected and, at the same time, a perfect evaluation of disturbances is impossible. Robustness is required to design a system through strong simplifications [7]. The choice of a Sliding Mode controller (SMC) [40][2], which is a well-established method for control of nonlinear systems, meets our need, especially with regard to uncertainty about the plant parameters. The

¹In rendezvous and docking manoeuvre (RVD), there is a spacecraft chaser that conducts a set of operations to reach a location closer to another satellite called target.

theory of variable structure system and sliding mode has been developed decades ago in the Soviet Union. The theory was mainly developed by Vadim I. Utkin [44] and David K. Young [50]. In sliding-mode control, the state is first driven towards a subset of the state space, the sliding set (sliding manifold). Subsequently, the state trajectory remains near the subset and moves asymptotically to a desired value, an equilibrium point. On the basis of the theory of sliding mode control, it should be robust, but experiments show that it has serious limitations. The main problem by applying the sliding mode is the input signal that shows small fluctuations of high frequency, this phenomenon is known as *chattering*, which strongly reduces the control performance. The chattering is a dangerous problem for moving mechanical parts. Moreover, it could mean a low control accuracy. Despite this, SMC is a popular control technique because it add robustness against unknown bounded disturbances. An High-order SMC (HOSMC) can be a solution to solve chattering problems. The control law mantain the same robustness characteristics but the chattering is very attenuated, HOSMC are able to drive to zero not only the sliding variable but also its $k - 1$ successive derivatives (k th-order sliding mode). In this way the chattering effect is significantly reduced.

Thanks to its effectiveness and simplicity to implement in practice, SMC has been widely employed for the attitude control and position dynamics for its ability to provide high performance and robustness. In [16] a first order sliding mode (FOSMC) was designed achieving good results in terms of accuracy and the chattering effect has been mitigated adding a saturation element. The same control technique (FOSMC) was developed in [15] to guide the position dynamics with a cluster of thrusters during a RVD scenario, showing good performance and a low fuel consumption was guaranteed. In the same work the attitude has been controlled by a second order SMC, a super twisting, in order to have a chattering reduction. Different applications can be found in literature. In [30] a different category of SMC has been implemented, a second order adaptive continuous twisting (ACTW), in which the controller gains are modulated in function of bounded uncertainties, including limitations of the actuation systems and of on-board hardware. The purpose is to ensure not only a chattering attenuation but also the adaptation of the gains to increase the operating range of the system. It was developed in order to analyze the effectiveness of the ACTW control methodology for both precise tracking of the attitude dynamics and for suppression of the structural vibration, which the mathematical model is derived by Lagrangian approach. The last part of this study proposes the problem of designing a dynamic controller capable of performing rest-to-rest manoeuvres for flexible spacecraft. Differently from [30] in literature can be found another way in [21] and [39] to evaluate disturbances caused by deformations of the appendages. The theme of flexibility is treated through the use of modal coordinates that defines the response in each normal-mode shape of the appendage obtained from a modal analysis.

Two SMC techniques are studied in this thesis: a Super Twisting SMC (STW) and

an ACTW SMC, which is based on the previous work [30]. The ACTW SMC is compared with the super-twisting SMC, which is widely used in space applications [40, 15, 42, 51], since it provides a continuous control law.

The SMC activates the actuators and controls the attitude actively. There are passive ways to have a desired attitude behaviour; they use the geometric, magnetic design of the satellite and the orbit properties to passively provide attitude stabilization and basic pointing, such as: gravity gradient stabilization, passive magnetic stabilization and aerodynamic stabilization in LEO². The active control requires actuators that can impart a torque to the spacecraft. We can divide them into two separate classes: reaction type actuators and momentum exchange devices. The first generates torques that can be considered external to the spacecraft so, reaction-type actuators have the ability to change the spacecraft angular momentum. Momentum exchange devices generate torques that can be considered internal to the spacecraft and don't change the overall angular momentum of the spacecraft. Reaction wheels, control moment gyros (CMG) and momentum wheels are momentum exchange devices. These actuators can provide high torque, angular momentum and slew rate capabilities to small satellites without any increase in power, mass or volume. The same actuators are analyzed in [46] where the paper explains how small satellites become more agile with CMGs. Agility considerably increases the operational envelope and efficiency of a spacecraft and significantly increases the return of Earth and science mission data [46]. A CMG consists of a spinning rotor and one or more motorized gimbals (Figure 1.1). The rotor rotates at a constant rate and the motor change the spinning axis so it modifies the angular momentum direction generating a torque in the opposite direction for the angular momentum conservation. An important issue to take into account is when the gimbal reaches a singularity condition which is the existence of some direction in the body in which the cluster is not capable of producing torque for a certain combination of gimbal angles. Various efforts have been made to overcome this troublesome problem, and many CMG singularity avoidance methods have been developed, with different advantages and disadvantages [26, 47, 27, 6].

The current thesis has the objective to design and implement a Sliding Mode Controller for a testbed³. The testbed is a platform with four Control Moment Gyros (CMGs) disposed in a pyramidal configuration mounted to test attitude software controls, which is illustrated in Figure 1.2. Several papers are focusing on the design of Sliding Mode Control (SMC) in which CMGs are used as actuation system. The authors of [13] propose a quaternion based first order sliding mode attitude controller for a spacecraft with Single Gimbal Control Moment Gyros (SGCMGs), in

²Low Earth Orbit

³As explained in abstract, a testbed is a platform for conducting rigorous, transparent, and replicable testing of scientific theories, computational tools and new technologies.

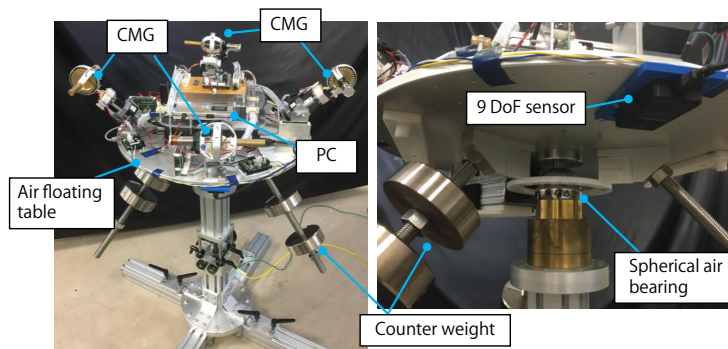


Figure 1.1. Testbed with 4 CMGs in pyramidal configuration

presence of uncertainties. The authors explains the advantages of using this robust control technique for attitude tracking and regulation. In [23, 24, 22] HOSMCs are applied on the attitude control system of nano-satellite TSUBAME, developed at University of Tokyo. [23] designed an HOSMCs in which uncertainties on the parameters are also included. Moreover, a modified steering logic based on two-norm and least-squares minimisation method is introduced for solving the singularity problem of CMGs.

In this thesis, the main idea is to directly control the gimbal rates, even if a steering law is considered. In [8] the steering law which is used in this thesis is implemented which directly generate the gimbal rates, to avoid the singularity problem.

The reliability of taking tests on testbeds is closely related to their capacity to emulate the peculiarities of the space environment, for instance, the frictionless rotational motion. Since the beginning of the space exploration, air bearing based platforms have been used as testbeds for simulating spacecraft attitude motion. The goal of this work is the rotational systems, which aim to provide a frictionless rotational movement with three degrees of freedom so, the testbed is equipped with a spherical air bearing and the platform rotates around it.

The main motivation for the choice of SMC is, as said before, its robustness against system uncertainties and disturbances. Particularly, the testbed focused in this thesis is affected by gravity torque caused by the center of mass (CoM) that is not in the same point of the center of bearing. This latter point created some issues at previous control laws (see [18, 8]), in fact three counter weights were added in order to get closer the CoM position to the center of bearing.

The function of the testbed is to test and choose computational efficient algorithm to be implemented on on-board systems. This is to ensure the capability to rapidly change the attitude of satellite with high slew rate, both to ensure the success of the mission and to avoid catastrophic impacts among crafts during a close approach.

These platforms are extremely important, they can provide a very low cost and low risk environment for evaluating the proposed design before launch.

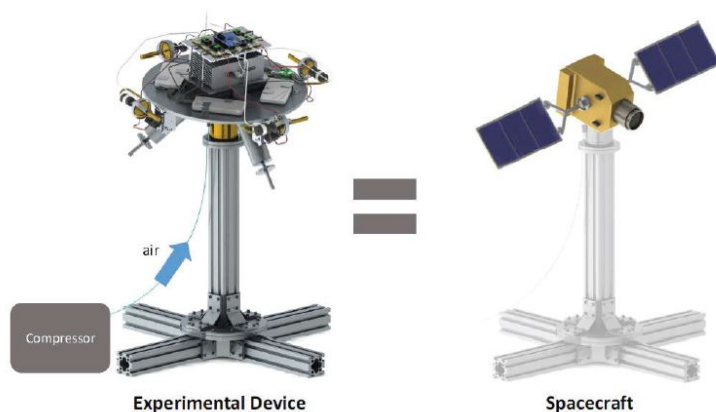


Figure 1.2. Experimental testbed that replicates the spacecraft attitude dynamics[8]

Different testbeds can be found in literature, to test control algorithms for different mission scenarios. Another important category of testbed is focused to test position dynamics controls during rendezvous manoeuvre. In [31] the performance of visual based navigation systems is verified. They are essential during close proximity operations, both in the role of primary devices and in the role of backup systems. Usually these tests are conducted by using a 2D free floating chaser platform equipped with a docking system and a camera dedicated to relative navigation with respect to a target platform. Both platforms have three degrees of freedom: the planar translation and rotation about the vertical axis, thanks to an air bearing which almost completely removes the sliding friction with respect to a smooth working surface. The image processing and filtering algorithms are processed to perform a relative navigation through a position controller.

1.1 Overview of the work

In the first chapter the work is introduced, with a focus on literature review and contribution. The second chapter includes the attitude dynamics and kinematics of a rigid spacecraft and it is applied to the testbed to describe its attitude motion. Furthermore, the principal reference frame are described to understand how to write the vector quantities in question. Finally the simulation environment is outlined.

In the third chapter the sliding mode techniques adopted are explained paying attention to their robustness. Then, the simulations of some manoeuvres are reported

and analyzed.

The last part of this work is focused to design an orbital simulator with the same testbed actuators where the behaviour of an orbiting spacecraft is emulated. The main purpose is testing the same control and actuators during a rendezvous manoeuvre adding a new disturbance created by solar panel flexibility.

Chapter 2

Attitude dynamics and CMG-based testbed

The key solution to the physics of attitude dynamics is considering our system as a rigid body, i.e. the distance between any two given points on it remains constant over time during the manoeuvre. This assumption makes the attitude problem easier. Such basic physical notions as angular kinetic energy, angular momentum, and moment about the center of mass are stated and used in the derivation of the fundamental laws of angular motion. These laws are based on Euler's moment equations and they are applied to analyze the testbed dynamics considering the torque generated by the 4 CMGs in a pyramidal configuration. We have to explain how to express the orientation of craft with respect to a reference frame, so, in the following chapter, the attitude has been described through the use of the four parameter quaternion representation. There exist also other attitude representation techniques such as the Euler angles, Gibbs vector, Cayley-Rodrigues vector, Modified Rodrigues parameter etc.

2.1 Reference frames

It's necessary to define how to write the physics quantities because all systems treated are moving, so, vectors rotate in space and change their coordinates with respect to a reference system. An inertial reference frame, a body one and a local reference system are used to study the spacecraft dynamics.

2.1.1 Inertial frame

In physics an inertial reference frame is a system where the first principle of dynamics is not violated. For example, in Newtonian celestial mechanics, taking the "fixed

stars” as a frame of reference, an inertial frame whose center is the center of mass of the solar system can be determined; relative to this frame, every acceleration of every planet can be considered (approximately) as a gravitational interaction with some other planet according to Newton’s laws of motion [12]. For our purpose, we consider the Earth a pseudo geocentric inertial frame, with the axis oriented to the fixed stars. The center of mass of the Earth is the origin of the reference frame, the **x-axis** lies in vernal equinox direction, towards a point in the constellation of Ares. The **z-axis** lies in Earth’s rotation axis, perpendicular to equatorial plane pointing in direction of the North Star. The **y-axis** finishes the triad of the reference system and it’s in the equatorial plane. This system is also called Earth-centered inertial (ECI) coordinate frame.

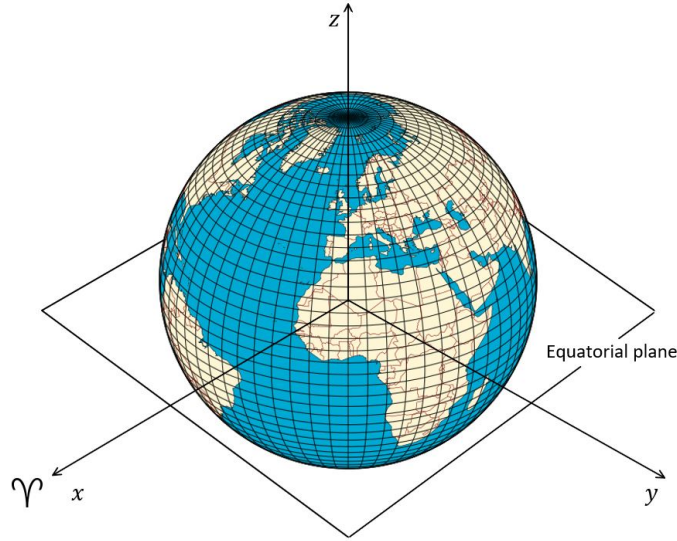


Figure 2.1. Earth Centered Frame [25]

2.1.2 Body reference frame

The body reference frame has the origin fixed to the center of mass of s/c (in our case, the testbed) and the axis coinciding with the principle direction of inertia but, generally, they can be taken according to the mission phase. This reference frame moves with the spacecraft in contrast to the inertial one and it’s possible to know the attitude angles thanks to an appropriate comparison with the inertial reference frame.

$$\mathbf{v}_{inertial} = \mathbf{L}_{BI}\mathbf{v}_{body} \quad (2.1)$$

In Equation 2.1 \mathbf{v}_{body} represents a vector in body reference frame, $\mathbf{v}_{inertial}$ is the

same vector in an inertial system and \mathbf{L}_{BI} is the rotation matrix between two systems.

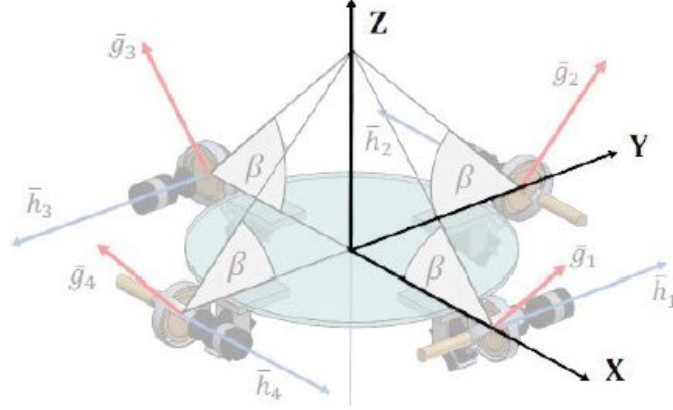


Figure 2.2. Body Reference Frame in CMG cluster [8]

2.1.3 LVLH frame

The last reference system is the spacecraft local frame or *Local Vertical Local Horizontal* (LVLH) frame. It is a local reference system and it is used during approach manoeuvres because it helps to describe the relative attitude motion. It is attached to the target spacecraft, as shown in Figure 2.3. This frame has basis $[V_{bar}, H_{bar}, R_{bar}]$ with R_{bar} lying along the radius vector from the Earth's center to the spacecraft, V_{bar} coinciding with the normal to the plane defined by the position and velocity vectors of the spacecraft and H_{bar} complete the triad and it is perpendicular to the orbital plane. The LVLH frame rotates with angular velocity vector ω , and its current orientation with respect to the ECI frame is given by another rotation matrix appropriately defined.

2.1.4 The quaternions

In this section Euler Angles doesn't treat but any rotation may be described using three angles and if the rotations are written in terms of rotation matrices D, C, and B, then a general rotation A can be written $A = BCD$. The three angles giving the three rotation matrices are called Euler angles (see Appendix A). They are easy to understand but they have a major deficiency, that it is possible, in some rotation sequences, to reach a situation where two of the three Euler angles cause rotation around the same axis of the object and the rotation reduces from three degrees of freedom to two. This situation is called "gimbal lock" [4]. Quaternions provide an alternative measurement technique that does not suffer from gimbal lock. Starting

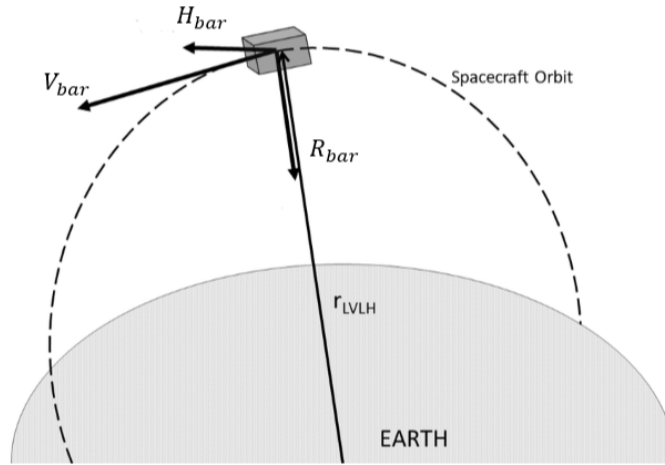


Figure 2.3. LVLH reference frame [36]

from Euler's eigenaxis rotation theorem states that it is possible to rotate a fixed frame F_I onto any arbitrary frame F_B with a simple rotation around an axis \hat{a} that is fixed in both frames, called the Euler's rotation axis or eigenaxis, the direction cosines of which are the same in the two considered frame, as explained in [1]. If we consider a generic vector \mathbf{v} and its rotation around \hat{a} as shown in Figure 2.4, we can write the relation (2.2) between the vectors \mathbf{v} and \mathbf{v}_{rot} .

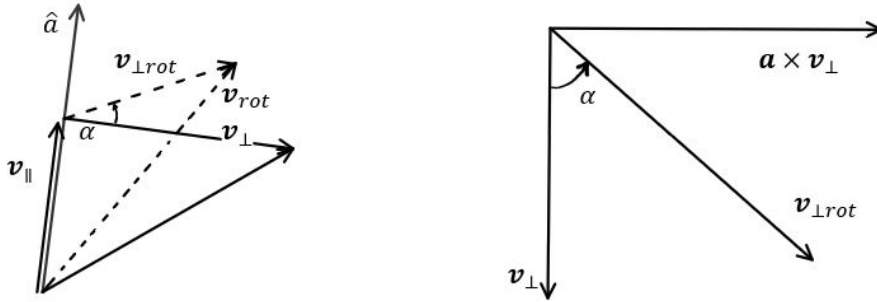


Figure 2.4. Euler's Theorem

$$\mathbf{v}_{rot} = \mathbf{v} \cos \alpha + (\mathbf{a} \cdot \mathbf{v})\mathbf{a}(1 - \cos \alpha) + \mathbf{a} \times \mathbf{v} \sin \alpha \quad (2.2)$$

The term \mathbf{v} is in each in any term so it's possible to group \mathbf{v} introducing a new term.

$$\mathbf{v}_{rot} = \mathbf{L}_{12}\mathbf{v} \quad (2.3)$$

$$\mathbf{L}_{12} = \cos \alpha \mathbf{I} + (1 - \cos \alpha) \mathbf{a}\mathbf{a}^T + \sin \alpha \mathbf{a}^\times \quad (2.4)$$

\mathbf{I} is the identity matrix.

$$\mathbf{a}^\times = \begin{bmatrix} 0 & -a_3 & a_2 \\ a_3 & 0 & -a_1 \\ a_1 & -a_2 & 0 \end{bmatrix} \quad (2.5)$$

The term \mathbf{a}^\times is the skewsymmetric matrix representing the vectorial product. \mathbf{L}_{12} is the rotation matrix between the two vectors and it can be used to express a vector in another reference system. Using the following equations (2.6) and (2.7) the final expression of \mathbf{L}_{12} is given by Eq. (2.8).

$$q_0 = \cos \frac{\alpha}{2} \quad (2.6)$$

$$\mathbf{q}_v = \mathbf{a} \sin \frac{\alpha}{2} \quad (2.7)$$

$$\mathbf{L}_{21} = (2q_0^2 - 1)\mathbf{I} + 2\mathbf{q}_v\mathbf{q}_v^T - 2q_0\mathbf{q}_v^\times \quad (2.8)$$

As shown in Eq. (2.8), the rotation matrix and kinematics (see Section 2.2.4) are purely algebraic, unlike axis-angle parameters and it is a great advantage.

2.2 Attitude dynamics

2.2.1 Euler's equation

Coming back to the introduction, the testbed is considered a rigid body. The second fundamental law of rigid body dynamics states that the time derivative of the angular momentum is equal to the sum of the external torque applied to the rigid body.

$$\frac{d\mathbf{h}}{dt} = \mathbf{M} \quad (2.9)$$

Writing the angular momentum \mathbf{h} in its components, considering that the body axis $\hat{\mathbf{i}}, \hat{\mathbf{j}}, \hat{\mathbf{k}}$ is rotating with angular velocity ω with respect to an inertial frame, the time derivative of the vector is:

$$\mathbf{h} = h_x \hat{\mathbf{i}} + h_y \hat{\mathbf{j}} + h_z \hat{\mathbf{k}} \quad (2.10)$$

$$\frac{d\mathbf{h}}{dt} = \dot{h}_x \hat{\mathbf{i}} + \dot{h}_y \hat{\mathbf{j}} + \dot{h}_z \hat{\mathbf{k}} + h_x \dot{\hat{\mathbf{i}}} + h_y \dot{\hat{\mathbf{j}}} + h_z \dot{\hat{\mathbf{k}}} \quad (2.11)$$

It is easily proved that:

$$\dot{\hat{\mathbf{i}}} = \boldsymbol{\omega} \times \hat{\mathbf{i}}; \quad \dot{\hat{\mathbf{j}}} = \boldsymbol{\omega} \times \hat{\mathbf{j}}; \quad \dot{\hat{\mathbf{k}}} = \boldsymbol{\omega} \times \hat{\mathbf{k}} \quad (2.12)$$

and therefore, keeping in mind that $\mathbf{h} = \mathbf{J}\boldsymbol{\omega}$, where $\mathbf{J} \in \mathbb{R}^{3 \times 3}$ is the inertia matrix.

$$\mathbf{M} = \dot{\mathbf{h}} + \boldsymbol{\omega} \times \mathbf{J}\boldsymbol{\omega} \quad (2.13)$$

The equation (2.13) is the Euler's equation [10, 32] and represents the basis for this treatment to describe the attitude dynamics of the testbed. Another way to write the Euler equation is:

$$\dot{\boldsymbol{\omega}} = \mathbf{J}^{-1}(\mathbf{M} - \boldsymbol{\omega} \times \mathbf{J}\boldsymbol{\omega}) \quad (2.14)$$

2.2.2 CMG-based spacecraft dynamic equation

A control moment gyroscope (CMG) is an attitude control device generally used in spacecraft attitude control systems. The CMG consists of a flywheel spinning at constant or variable rate (in this thesis it is fixed) and a motorized gimbal that tilts the rotor's angular momentum. As the rotor tilts, the changing angular momentum causes a gyroscopic torque that rotates the spacecraft in the opposite direction of tilt. This happens for the angular momentum conservation because the external moment acting on the system is null, it is an internal torque. At least three CMGs are necessary for a three-axis control, but four is ideal for redundancy. A pyramidal configuration is mounted on the testbed as shown in Figure 2.5.

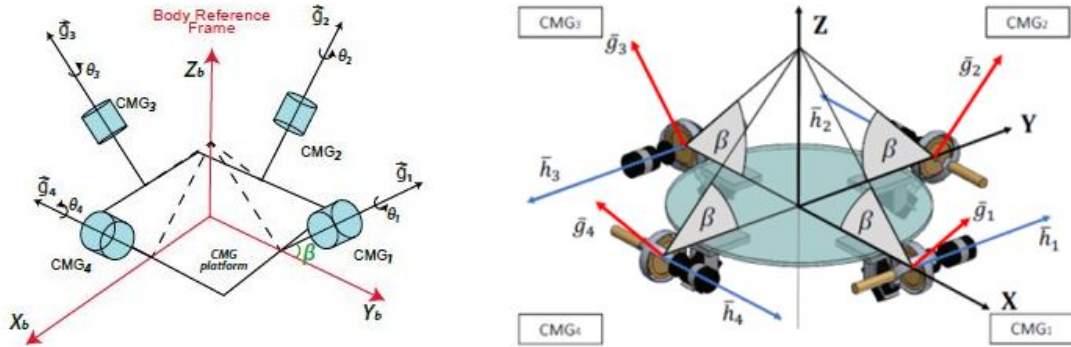


Figure 2.5. Configuration of a pyramidal testbed equipped with 4 CMGs [33][18]

β is the skew angle, fixed over time, θ is the gimbal angle, it changes over time. \mathbf{g} and \mathbf{h} are the gimbal vector and angular momentum vector of each CMG. The torque vector \mathbf{c} is the cross product between them:

$$\mathbf{c} = \mathbf{g} \times \mathbf{h} \quad (2.15)$$

Starting from the equation (2.13), the total angular momentum can be split into two terms [41], as follows

$$\mathbf{M}_B = \dot{\mathbf{h}}_B + \boldsymbol{\omega}_B \times \mathbf{h}_B \quad (2.16)$$

$$\mathbf{h}_B = \mathbf{h}_B^C + \mathbf{J}_B \boldsymbol{\omega}_B \quad (2.17)$$

where:

- The subscript $(\cdot)_B$ indicates that the vector is expressed in the Body Reference Frame;
- $\mathbf{h}_B \in \mathbb{R}^3$ indicates the total angular momentum of the spacecraft;
- $\mathbf{h}_B^C \in \mathbb{R}^3$ refers only to the CMG system;
- $\dot{\mathbf{h}}_B \in \mathbb{R}^3$ is the time derivative of the total angular momentum of the system.

\mathbf{h}_B^C can be factored as function of the angular momentum of each wheel and of the gimbal angle

$$\mathbf{h}_B^C = h_w \sum_{i=1}^4 \mathbf{h}_i(\theta_i) \quad (2.18)$$

with

$$\begin{aligned} \mathbf{h}_1(\theta_1) &= \begin{bmatrix} -\sin(\theta_1)\cos\beta \\ \cos(\theta_1) \\ \sin(\theta_1)\sin\beta \end{bmatrix}, & \mathbf{h}_2(\theta_2) &= \begin{bmatrix} -\cos(\theta_2) \\ -\sin(\theta_2)\cos\beta \\ \sin(\theta_2)\sin\beta \end{bmatrix}, \\ \mathbf{h}_3(\theta_3) &= \begin{bmatrix} \sin(\theta_3)\cos\beta \\ -\cos(\theta_3) \\ \sin(\theta_3)\sin\beta \end{bmatrix}, & \mathbf{h}_4(\theta_4) &= \begin{bmatrix} \cos(\theta_4) \\ \sin(\theta_4)\cos\beta \\ \sin(\theta_4)\sin\beta \end{bmatrix} \end{aligned} \quad (2.19)$$

$\theta_i \in \mathbb{R}$ is the gimbal angle, for $i = 1, \dots, 4$, and $h_w = J_w \omega_w \in \mathbb{R}$ denotes the angular momentum of each wheel (constant). After having introducing the relations written previously, the Euler's equation becomes:

$$\mathbf{M}_B = \boldsymbol{\omega} \times (\mathbf{J}_B \boldsymbol{\omega}_B + \mathbf{h}_B^C) + \mathbf{J}_B \dot{\boldsymbol{\omega}}_B + \dot{\mathbf{h}}_B^C \quad (2.20)$$

The control input $\mathbf{u} \in \mathbb{R}^3$ can be defined as function of the time derivative of \mathbf{h}_B^C

$$\mathbf{u} = -\dot{\mathbf{h}}_B^C - \boldsymbol{\omega} \times \mathbf{h}_B^C \quad (2.21)$$

For a cluster of four CMGs, the internal momentum vector \mathbf{h}_B^C and $\dot{\mathbf{h}}_B^C$ are functions of the rotation angle θ_i of each wheel about their gimbal axis, so

$$\dot{\mathbf{h}}_B^C = h_w \mathbf{A}(\boldsymbol{\theta}) \dot{\boldsymbol{\theta}} \quad (2.22)$$

hence, the desired control torque can be switched into a command for CMGs in order to have an attitude control by tracking $\dot{\boldsymbol{\theta}}$. $\dot{\boldsymbol{\theta}} \in \mathbb{R}^4$ is the gimbal rate and it is given by:

$$\dot{\boldsymbol{\theta}} = \frac{1}{h_w} \mathbf{A}^T (\mathbf{A} \mathbf{A}^T)^{-1} (-\mathbf{u} - \boldsymbol{\omega} \times \mathbf{h}_B^C) \quad (2.23)$$

in which $\mathbf{A}(\boldsymbol{\theta}) \in \mathbb{R}^{3 \times 4}$ transforms the four-component vector derived from CMG cluster in body axes and considering $s\beta = \sin \beta$ and $c\beta = \cos \beta$, it is

$$\mathbf{A}(\boldsymbol{\theta}) = \begin{bmatrix} -c\beta \cos \theta_1 & \sin \theta_2 & c\beta \cos \theta_3 & -\sin \theta_4 \\ -\sin \theta_1 & -c\beta \cos \theta_2 & \sin \theta_3 & c\beta \cos \theta_4 \\ s\beta \cos \theta_1 & s\beta \cos \theta_2 & s\beta \cos \theta_3 & s\beta \cos \theta_4 \end{bmatrix} \quad (2.24)$$

At the end, under the assumptions:

- The initial angular momentum is zero;
- The initial torque applied to the body is zero, $\mathbf{M}_B(0) = 0$.

The dynamic equation can be rewritten as

$$\dot{\boldsymbol{\omega}}_B = -h_w \mathbf{J}_B^{-1} \mathbf{A}(\boldsymbol{\theta}) \dot{\boldsymbol{\theta}} \quad (2.25)$$

Singular direction avoidance steering law (SDA)

The matrix $\mathbf{A}(\boldsymbol{\theta})$ is not square so, there could be the presence of singularity that may not lead the problem to a convex solution. A singularity is encountered when there exists some direction in the body in which the cluster is not capable of producing torque for a certain combination of gimbal angles. At each singular state, all admissible torque directions lie on a 2D surface in the 3D space; therefore, the CMG system cannot generate a torque perpendicular to this surface. The CMG singularities can be classified into two categories:

- *external* or *saturated* singularities occur when the sum of all CMG angular momenta lies on a maximum momentum surface;
- *internal* singularities occur when the total momentum lies inside this envelope;

Working near these singularities can lead in unacceptably high gimbal rate commands and undesirable system response if one requires to generate a torque in the singular direction.

A steering law, as in [8] is introduced in order to avoid singularity conditions.

$$\dot{\theta} = \frac{1}{h_w} \mathbf{A}^T (\mathbf{A} \mathbf{A}^T + \lambda \mathbf{u}_3 \mathbf{u}_3^T)^{-1} \dot{\mathbf{h}}_B^C \quad (2.26)$$

where λ is a positive scalar parameter related to the SDA steering law and $\mathbf{u}_3 \in \mathbb{R}^3$ denotes the eigenvector corresponding to the smallest singular value of \mathbf{A} .

2.2.3 Gravity torque disturbance

The main disturbance related to this experimental setup is the torque caused by a misalignment between the center of rotation and the center of gravity of the testbed. In order to minimize this gravity effect, the experimental setup is equipped with three counter weights, which are attached to the testbed by ball screws. The position of the three counter weights has to be adjusted manually, hence it is difficult to obtain a perfect alignment of the center of gravity and of the center of rotation. During manoeuvring, the center of gravity moves, so its position changes with time altering the moment arm. The starting vector which represents the deviation of the center of gravity in the body frame is experimentally estimated as:

$$\boldsymbol{\rho} = [-10, 5, -30] \mu m [11] \quad (2.27)$$

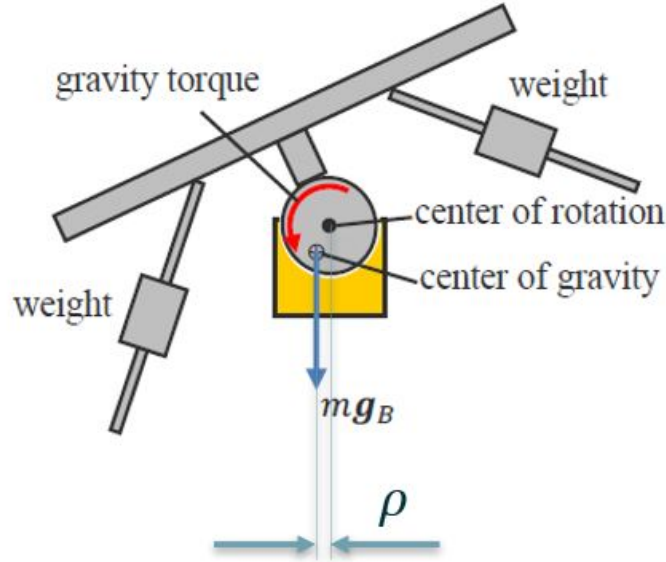


Figure 2.6. Gravity torque in the experimental setup [11]

In order to always have the right gravity torque, the vector $\boldsymbol{\rho} \in \mathbb{R}^3$ is multiplied by rotation matrix \mathbf{L}_{IB} (Eq. (2.1)), so it can be converted in body axis taking into account the rotation of the testbed.

$$\begin{aligned}\tilde{\boldsymbol{\rho}} &= \mathbf{L}_{BI}^{-1}\boldsymbol{\rho} \\ \mathbf{M}_G &= m\tilde{\boldsymbol{\rho}} \times \mathbf{g},\end{aligned}\tag{2.28}$$

in which \mathbf{g} is the acceleration of gravity.

2.2.4 Kinematic equation of motion

In chapter 2.1.4 quaternions are introduced and it is necessary to know their values over the period of the mission. In section 2.2.2 the equation of $\dot{\boldsymbol{\omega}}_B$ has been obtained, hence it takes a connection between $\boldsymbol{\omega}$ and q . As explained in [32], starting from the equations (2.6) and (2.7), their time derivatives are

$$\dot{q}_0 = -\frac{1}{2}\mathbf{q}_v^T\boldsymbol{\omega}_B\tag{2.29}$$

$$\dot{\mathbf{q}}_v = \frac{1}{2}(q_0\mathbf{I} + \mathbf{q}_v^\times)\boldsymbol{\omega}_B\tag{2.30}$$

Now we can write them in the form of a system equation [32]:

$$\frac{d\mathbf{q}}{dt} = \dot{\mathbf{q}} = \frac{1}{2}\boldsymbol{\Gamma}(q)\boldsymbol{\omega}_B\tag{2.31}$$

with $\mathbf{q} = [q_0, \mathbf{q}_v^T]^T = [q_0, q_1, q_2, q_3]^T \in \mathbb{R}^4$, where $\mathbf{q}_v = [q_1, q_2, q_3]^T \in \mathbb{R}^3$ is the vectorial part of the quaternion, and q_0 is the scalar term. The matrix $\boldsymbol{\Gamma}(q) \in \mathbb{R}^{4 \times 3}$ is composed by:

$$\boldsymbol{\Gamma}(q) = \begin{bmatrix} q_4 & -q_3 & q_2 \\ q_3 & q_4 & -q_1 \\ -q_2 & q_1 & q_4 \\ -q_1 & -q_2 & -q_3 \end{bmatrix}\tag{2.32}$$

2.3 Simulation environment

The software used for the modeling and the analysis of the testbed dynamics is the *MathWorks* product *Simulink*, with the support of *Matlab* to initialize the variables and change the constant parameters.

As shown in Figure 4.9, the model is organised into subsystems in order to maintain a well-defined structure. Within these subsystems the equations described in the previous sections are implemented. Each block has a specific task, for example the

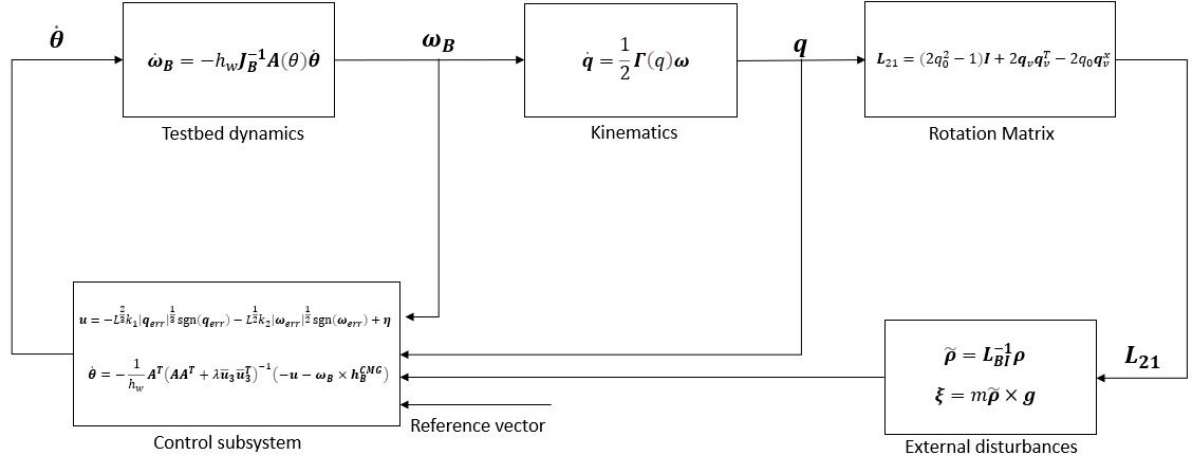


Figure 2.7. Simulink scheme

control block calculates the input for CMG cluster. The most important subsystem is the control block, because it was designed based on the quantities that the $C++$ code that runs on the testbed provides as a measure of the states. This is to have a proper implementation when the Simulink code will be translated into $C++$. The principal testbed physical properties and input constraints are given in the following tables:

Variable	Nomenclature	Numerical value	Units									
Mass of testbed	m	21.2	kg									
Inertia matrix	J	<table border="1" style="display: inline-table; vertical-align: middle;"> <tr> <td>0.464</td> <td>0</td> <td>0</td> </tr> <tr> <td>0</td> <td>0.534</td> <td>0</td> </tr> <tr> <td>0</td> <td>0</td> <td>0.610</td> </tr> </table>	0.464	0	0	0	0.534	0	0	0	0.610	kg/m^2
0.464	0	0										
0	0.534	0										
0	0	0.610										
Angular momentum of each wheel	h_w	0.0576	$kg\ m^2/s$									
Skew angle	β	45	deg									

Table 2.1. Physical properties of the testbed

Furthermore, in all simulations the initial condition of the state $x = [q, \omega]$ and of the gimbal angles θ are:

Variable	Nomenclature	Numerical value	Units
Gimbal motors speed			
max value	$\bar{\theta}$	1	<i>rad/s</i>
Acceleration constraints			
on the CMG motors	$\bar{\ddot{\theta}}$	2	<i>rad/s²</i>
Angular velocity constraint			
of the testbed	$\bar{\omega}$	25	<i>deg/s</i>

Table 2.2. Input constraint

$$\theta(0) = \begin{bmatrix} 0 \\ 0 \\ 0 \\ 0 \end{bmatrix} \quad x(0) = \begin{bmatrix} 1 \\ 0 \\ 0 \\ 0 \\ 0 \\ 0 \\ 0 \end{bmatrix} \quad (2.33)$$

Chapter 3

Sliding Mode control (SMC)

3.1 Introduction to control theory

The theory of control is the branch of maths and engineering that studies the behaviour of dynamical systems in which their parameters are subject to time variations. The automatic control aims to manipulate input variables to change the behaviour of the system through a command input. Any dynamic system with a finite dimension can be described by a set of first differential equation. The simplest system to analyze is the 1D mass-spring-damper model depicted in Figure 3.1.

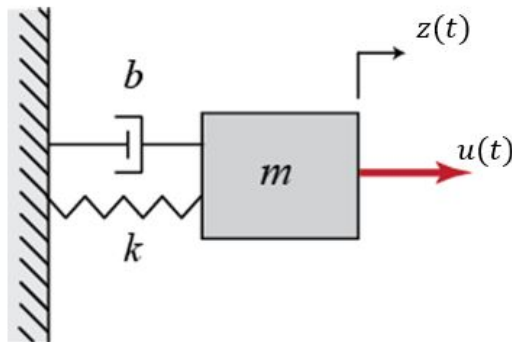


Figure 3.1. Mass spring damper 1D model

$$m\ddot{z} + b\dot{z} + kz = u(t) \quad (3.1)$$

The first differential equation is obtained by introducing the variable $x_1 = z$ so $x_2 = \dot{z}$. The system (3.2) can be written as:

$$\dot{x} = \begin{bmatrix} \dot{x}_1(t) \\ \dot{x}_2(t) \end{bmatrix} = \begin{bmatrix} x_2(t) \\ -\frac{k}{m}x_1(t) - \frac{b}{m}x_2(t) + \frac{1}{m}u(t) \end{bmatrix} \quad (3.2)$$

a compact form of the system (3.2) is:

$$\dot{x} = Ax + Bu \quad (3.3)$$

in which x is the state vector that completely describes the system and, in this case, it is the mass displacement and its velocity. u is the input the control action to modify the system behaviour. Now, we introduce the system output y (3.4) which is the variables that drop off the system and, in a *closed loop control*, they will be measured to get compared with a reference signal.

$$y = Cx + Du \quad (3.4)$$

If the terms A, B, C and D remain constant over time, the system is Linear time-invariant (LTI). A system written in this form is linear so, it is composed by linear equations. While dynamical systems, which in general is non-linear, do not have closed-form solutions, linear systems can be solved exactly. Linear systems can also be used to understand the qualitative behavior of general dynamical systems, by calculating the equilibrium points of the system and approximating it as a linear system around those point.

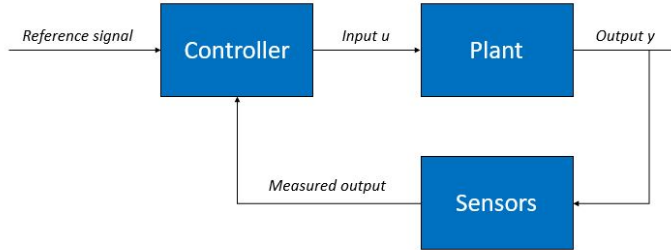


Figure 3.2. Block diagram representation of a closed loop control system

Figure 3.2 shows a simplified scheme of the mathematical model developed in this thesis. The plant is the system where there are a relation between inputs and outputs and this particular case is represented by the spacecraft (or the testbed). What has been said above represents the simplest case, the system is LTI and no disturbances working on it.

3.1.1 Introduction to SMC

In the development of any practical control problem, there will be always a discrepancy between the real plant and its mathematical model used for controller

design. These differences grow when external disturbances and neglected parameters are added. The theory of Sliding Mode Control and other robust controls have as their purpose to solve this problem. Furthermore, systems are usually approximated as linear around an equilibrium point neglecting non-linearities but this isn't a source of errors because SMC is a non-linear control. Hence the major advantage of sliding mode is low sensitivity to plant parameter variations and disturbances which eliminates the necessity of exact modeling. The control seeks to achieve the aim forcing the feedback system to reach a regime of *Sliding mode* that is typical in a Variable structure system (VSS)[50]. Theoretically, once reached the Sliding Mode, the system will always stay in those conditions, even with the presence of disturbances and model errors. These ideal conditions are maintained introducing a control signal at infinite frequency. In the real case the system trajectory ranges around to the sliding surface (*chattering*) and the width of fluctuation depends on the frequency, in inverse proportion. A first example of a sliding mode control can be done taking into consideration the 1D mass-spring-damper model introduced in Eq. (3.1).

$$\ddot{z} + a\dot{z} + dz = u \tag{3.5}$$

in which $a = \frac{b}{m}$ and $d = \frac{k}{m}$. We need to reach the *sliding mode* and our purpose is the equilibrium point where $z = 0$ and $\dot{z} = 0$. A sliding manifold can be chosen such as [40, 3]:

$$\sigma = cz + \dot{z} \tag{3.6}$$

Then, a control input u can be selected as:

$$u = -K|z|sign(\sigma) \tag{3.7}$$

where K is a positive constant to be appropriately chosen and $sign(s)$ is a function where its value is 1 if $\sigma > 0$ and -1 if $\sigma < 0$. The input vector makes sure to take the system on the line $\sigma = 0$ and when the trajectory reaches it, the only dynamics law is $cz + \dot{z}$ so, the system aims at the origin, sliding on the manifold $\sigma = 0$. If K is big enough, sliding mode condition is insensitive to disturbances. The trajectory can be represented on the state plane illustrated in Figure 3.3 [3].

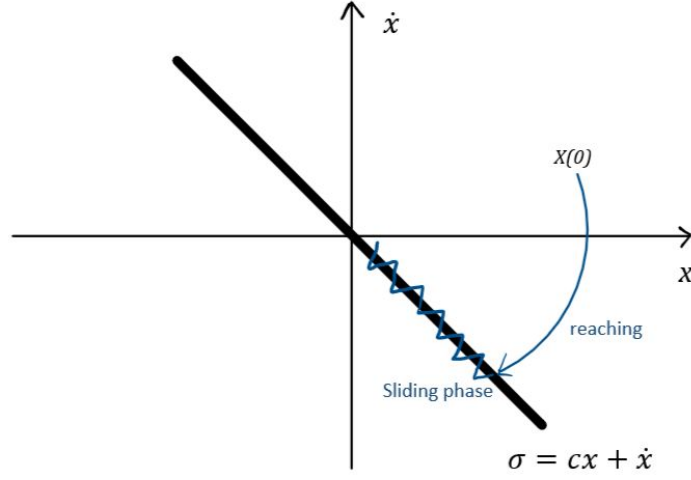


Figure 3.3. Trajectory on the state plane

3.1.2 Design of sliding mode control

A SISO (Single Input Single Output) system can be written similarly to Eq. (3.3):

$$\mathbf{x}^{(n)} = f(\mathbf{x}, t) + B(\mathbf{x}, t)u + d(t) \quad (3.8)$$

The superscript $(\cdot)^n$ indicates the grade of the system, so $\mathbf{x} = [x, \dot{x}, \ddot{x} \dots x^{(n-1)}]$. In Eq. (3.8) the term Ax is replaced by $f(\mathbf{x}, t)$ because we are considering the general case so, in a non-linear system, it is not possible to make explicit the vector \mathbf{x} . Furthermore, $f(\mathbf{x}, t)$ and $B(\mathbf{x}, t)$ are not known a priori and $d(t)$ is a limited disturbance. The purpose is to solve the problem of trajectory tracking $x_d(t) = [x_d, \dot{x}_d \dots x_d^{n-1}]$ in a robust way with respect to d and uncertainty about f and b . We write an error trajectory $\mathbf{e} = \mathbf{x} - \mathbf{x}_d$ in order to define the time-variant surface $\sigma(t)$ as in [3]:

$$\sigma(\mathbf{e}, t) = \left(\frac{d}{dt} + \lambda \right)^{n-1} e = 0, \quad \lambda > 0 \quad (3.9)$$

The typical case is $n = 2$, so:

$$\sigma = \dot{e} + \lambda e \quad (3.10)$$

The scalar function $\sigma(\mathbf{e}, t)$ is a measure of tracking error, so it is necessary to limit it to keep \mathbf{e} and its derivatives small. The problem of trajectory tracking becomes making invariant and attractive $\sigma(t) = 0$, so σ^2 , what is a measure of distance between a state \mathbf{x} and σ , is decreasing on all trajectories.

The second order dynamics ($n = 2$) is considered:

$$\ddot{x} = f(x, \dot{x}, t) + u \quad (3.11)$$

f is not known for certain. A function \hat{f} was estimated, then the error is restricted by a known function $F(x, \dot{x}, t)$:

$$|\hat{f} - f| \leq F \quad (3.12)$$

Our purpose is to define a control law by applying Lyapunov function techniques [40] to the σ -dynamics that is derived from Eq. (3.10), in which the sliding manifold $\sigma = 0$ must be made invariant.

$$\dot{\sigma} = \ddot{x} - \ddot{x}_d + \lambda \dot{e} = f + u - \ddot{x}_d + \lambda \dot{e} = 0 \quad (3.13)$$

For the σ -dynamics a candidate Lyapunov function is introduced taking the form:

$$V = \frac{1}{2}\sigma^2 \quad (3.14)$$

In order to achieve finite-time convergence of Eq. (3.13), the following inequality must be satisfied:

$$\dot{V} = \frac{1}{2} \frac{d}{dt} \sigma^2 \leq -\eta |\sigma| \quad (3.15)$$

If the initial condition $x(t_0) \neq x_d(t_0)$, the surface σ is reached in a finite time less than $|\sigma(t_0)|/\eta$.

If we reconsider Eq. (3.13) and bearing in mind that f is not known precisely, an ideal control is:

$$\hat{u} = \ddot{x}_d - \hat{f} - \lambda \dot{e} \quad (3.16)$$

It is necessary to add a discontinuous term to enforce the system to stay in the sliding mode regime on $\sigma = 0$. In order to ensure robustness against disturbances and uncertainties, a high gain function must be used, so a discontinuous function $sign(\sigma)$ is added to the term \hat{u} . The proportional coefficient k must be chosen in order to verify the inequality Eq. (3.15).

$$\frac{1}{2} \frac{d}{dt} \sigma^2 = \dot{\sigma} \cdot \sigma = [f - \hat{f} - k sign(\sigma)] \cdot \sigma = (f - \hat{f})\sigma - k|\sigma| \leq -\eta |\sigma| \quad (3.17)$$

Thus, for Eq. (3.12) it is simple to write $k \geq F + \eta$. If there are some disturbances $d(t)$ that affects dynamics limited by a constant upper bound D (so $|d(t)| \leq D$), the final relation that ensures a SMC robust against disturbances and uncertainties is:

$$k \geq F + D + \eta \quad (3.18)$$

As deeply explained in [3].

3.2 Super-twisting SMC

In Section 3.1.1 a discontinuous high frequency sliding mode is introduced which leads the sliding variable to zero in a finite time even if there are disturbances and uncertainties by choosing the gain k appropriately. In many cases high-frequency switching control is impossible to apply and continuous control is necessary. To avoid these restrictions, a natural solution is the application of the SMC with high-order control structure. The super-twisting sliding mode control (STW) is a second-order control structure and characterized by the following advantages:

- The effect of chattering with STW is reduced compared to classical first-order SMC techniques [28, 40];
- The STW steers to zero both the sliding surface σ and its first time derivative $\dot{\sigma}$ in finite time [17].
- The controller does not need measurements of $\dot{\sigma}$.

Considering the following dynamic system similiar to Eq. (3.8):

$$\dot{\sigma} = f(t, x) + B(t, x)u \quad (3.19)$$

Then, the positive constants C, K_M, K_m, U_M, q must meet the following conditions:

$$\dot{f} + U_M|\dot{B}| \leq C, \quad 0 \leq K_m \leq B(t, x) \leq K_M, \quad |f/B| < qU_M, \quad 0 < q < 1 \quad (3.20)$$

Now, we can define the Super Twisting sliding mode:

$$\begin{cases} u = -\lambda|\sigma|^{1/2}sign(\sigma) + w \\ \dot{w} = \alpha sign(\sigma) \end{cases} \quad (3.21)$$

With $K_m\alpha > C$ sufficiently large, the controller (3.21) ensures the appearance of a 2-sliding mode $\sigma = \dot{\sigma} = 0$ in system (3.19), which attracts the trajectories in finite time. The control u enters in finite time the segment $[-U_M, U_m]$ and never leaves the segment, if the initial value is inside at the beginning, as deeply detailed in [40]. A sufficient condition for validity of the theorem is:

$$\lambda > \sqrt{\frac{2}{(K_m\alpha - C)}} \frac{(K_m\alpha + C)K_M(1 + q)}{K_m^2(1 - q)} \quad (3.22)$$

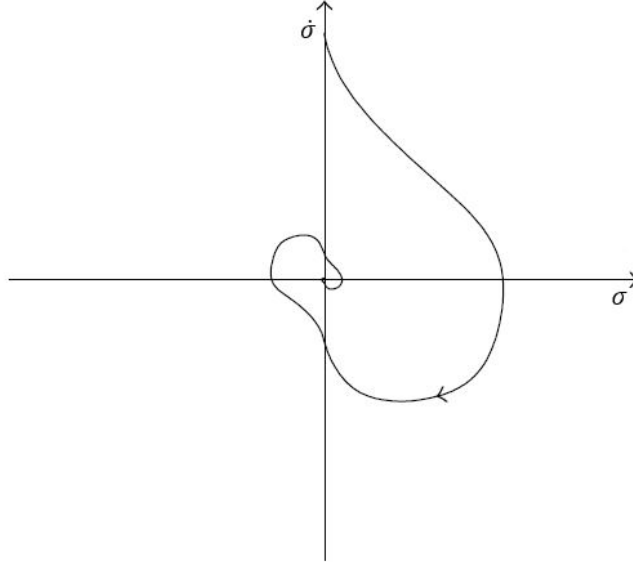


Figure 3.4. Phase plane trajectory of Super-twisting algorithm [40] (pp 156)

Figure 3.4 graphically represents the trajectory of STW SMC described above. One of the two techniques of SMC developed in this work is a Super-twisting. The first passage is to find the state vectors which compose the sliding surface. The purpose is tracking the spacecraft rotational dynamics so, an attitude and an angular velocity state vectors are necessary to provide a complete attitude control. In order to describe the attitude, we use quaternions explained in Section 2.1.4 but, the general goal of control is to make the state vector track some reference vector, so it is necessary to measure the distance between the reference and the actual state. For this purpose we define:

- *the angular velocity tracking error*

$$\tilde{\omega} = \omega_r - \omega \quad (3.23)$$

- *the quaternion tracking error*

$$\tilde{\mathbf{q}} = \begin{bmatrix} \tilde{q}_0 \\ \tilde{\mathbf{q}} \end{bmatrix} = \mathbf{q}^{-1} \otimes \mathbf{q}_r \quad (3.24)$$

The subscript $(\cdot)_r$ indicates the reference vector and the symbol \otimes shows the quaternion multiplication.

$$\mathbf{p} = \mathbf{q} \otimes \mathbf{r} = \begin{bmatrix} p_0 \\ p_1 \\ p_2 \\ p_3 \end{bmatrix} = \begin{bmatrix} q_0 & -q_1 & -q_2 & -q_3 \\ q_1 & q_0 & -q_3 & q_2 \\ q_2 & q_3 & q_0 & -q_1 \\ q_3 & -q_2 & q_1 & q_0 \end{bmatrix} \cdot \begin{bmatrix} r_0 \\ r_1 \\ r_2 \\ r_3 \end{bmatrix} \quad (3.25)$$

Furthermore, the quaternion inverse:

$$\mathbf{q}^{-1} = [q_0 \quad -q_1 \quad -q_2 \quad -q_3]^T \quad (3.26)$$

Thus the sliding surface is a function of these two parameters and it is defined as:

$$\boldsymbol{\sigma}(\mathbf{q}, \boldsymbol{\omega}, t) = \tilde{\boldsymbol{\omega}} + k\tilde{\mathbf{q}} \quad (3.27)$$

According to [45, 37], the performance of sliding mode controllers can be improved including the equivalent control $\mathbf{u}_{eq} \in \mathbb{R}^3$ in the control law definition. It consists in a relation between the control input $\mathbf{u}_s \in \mathbb{R}^3$ and the system dynamics when the sliding mode is reached. Thus, including the equivalent control makes the sliding surface to be *invariant*. So, the control law applied to the system is the sum of two contributions

$$\mathbf{u} = \mathbf{u}_s + \mathbf{u}_{eq}.$$

Starting from the definition of the first time derivative of the sliding surface and substituting $\dot{\boldsymbol{\omega}}$ of Eq. ((2.16)),

$$\dot{\boldsymbol{\sigma}} = \dot{\boldsymbol{\omega}}_r - \dot{\boldsymbol{\omega}} + k\dot{\tilde{\mathbf{q}}} = \dot{\boldsymbol{\omega}}_r + \mathbf{J}^{-1}\boldsymbol{\omega} \times \mathbf{J}\boldsymbol{\omega} - \mathbf{J}^{-1}\mathbf{u} + \frac{k}{2}[\tilde{q}_0\tilde{\boldsymbol{\omega}} + \tilde{\mathbf{q}} \times (\boldsymbol{\omega}_r + \boldsymbol{\omega})] = 0$$

A crucial step was made by replacing $\dot{\boldsymbol{\omega}}$ with its expression obtained from (2.14), the term \mathbf{M}_B is replaced by the input torque \mathbf{u} , as explained in [37].

$$\mathbf{u}_{eq} = \mathbf{J} \left[\dot{\boldsymbol{\omega}}_r + \frac{k}{2}[\tilde{q}_0\tilde{\boldsymbol{\omega}} + \tilde{\mathbf{q}} \times (\boldsymbol{\omega}_r + \boldsymbol{\omega})] \right] + \boldsymbol{\omega} \times \mathbf{J}\boldsymbol{\omega} \quad (3.28)$$

Then, a further term obtained from Eq. 3.21 is added to make the sliding surface *attractive*. The complete control law is:

$$\begin{cases} \mathbf{u} = \mathbf{u}_{eq} - \lambda|\boldsymbol{\sigma}|^{1/2}sign(\boldsymbol{\sigma}) + \mathbf{w} \\ \dot{\mathbf{w}} = \alpha sign(\boldsymbol{\sigma}) \end{cases} \quad (3.29)$$

3.3 Adaptive continuous Twisting (ACTW)

In Section 1, we introduced the ACTW sliding mode control. Starting from the works [40, 34, 43] the adaptive continuous twisting has as main feature the capability to change its gains, specifically, the adaptive control is a set of techniques that

permit to adjust the value of control parameters in real time to monitor controlled variables even if plant parameters are unknown or if they change over time. This capability increases the robustness even more because if disturbances rise over time, there's an adjustment of gains that cover this growth. The adjustment is important because if the gains are greater a priori, a great input control is always given to the actuators so, they would work badly.

Considering the kinematic equation (2.31) and manipulating the Euler equation 2.14, the following equation is obtained:

$$\begin{cases} \dot{\mathbf{q}} = \frac{1}{2}\mathbf{\Gamma}(q)\boldsymbol{\omega} \\ \dot{\boldsymbol{\omega}} = \mathbf{J}^{-1}(\mathbf{u} - \boldsymbol{\omega} \times \mathbf{J}\boldsymbol{\omega}) + \mathbf{d}(t) \end{cases} \quad (3.30)$$

According to the system (3.30), a continuous twisting SMC can be designed as in [30]:

$$\begin{cases} \mathbf{u}_s = -k_1|\tilde{\mathbf{q}}|^{\frac{1}{3}}\text{sign}(\tilde{\mathbf{q}}) - k_2|\boldsymbol{\omega}_{err}|^{\frac{1}{2}}\text{sign}(\boldsymbol{\omega}_{err}) + \boldsymbol{\eta} \\ \dot{\boldsymbol{\eta}} = -k_3|\tilde{\mathbf{q}}|\text{sign}(\tilde{\mathbf{q}}) - k_4|\boldsymbol{\omega}_{err}|\text{sign}(\boldsymbol{\omega}_{err}) \end{cases} \quad (3.31)$$

Since in practical cases the Lipschitz disturbances are usually bounded by $\dot{d}(t) \leq \mu^* = L\mu$, control gains can be scaled as follows [43]:

$$k_{p1} = k_1L^{\frac{2}{3}} \quad k_{p2} = k_2L^{\frac{1}{2}} \quad k_{p3} = k_3L \quad k_{p4} = k_4L \quad (3.32)$$

Gains k_i can be substituted by k_{pi} . The adaptation mechanism consisting in varying the gain L , as in [30]:

$$\begin{aligned} \dot{L}(t) &= l, & \text{if } |\mathbf{x}_e(t)| > \epsilon & \text{ and } L(t) < L_{max} \\ \dot{L}(t) &= 0, & \text{if } |\mathbf{x}_e(t)| \leq \epsilon & \text{ and } t - t_0 < \tau \\ \dot{L}(t) &= -l, & \text{if } |\mathbf{x}_e(t)| \leq \epsilon & \text{ and } t - t_0 > \tau \text{ and } L(t) > L_{min} \end{aligned} \quad (3.33)$$

l is a positive constant, $\mathbf{x}_e(t) = [\mathbf{q}_e, \boldsymbol{\omega}_e]^T$ is the state error. When the state error exceeds the required tolerance ϵ , L grows until $|\mathbf{x}_e(t)|$ returns to be less than ϵ . After that, if the state errors remain less than ϵ for a time equal to τ , L starts to decrease. The value of l must be chosen in order to compensate the growth of disturbances \dot{d} as detailed in [14, 30].

3.4 Simulation results

The performance of the proposed control laws are tested in simulations, starting from the characteristics of the testbed. The testbed simulates a spacecraft using a metal plate equipped with the four CMGs in pyramidal configuration, a PC, two microcomputers, and three sets of counter weights, as detailed in [11]. The

principal testbed physical properties and input constraints are given in the Table 2.1. Hardware limitations and limited frequency of control laws are included in the simulations. The constraints of the testbed are included to simulate the real behaviour of the system and test the performance and the computational effort for on-board implementations. The simulations have a total duration of 20 seconds. The angular velocity reference has a trapezoidal shape, where for the first 5 seconds, the testbed increases its angular velocity, then it remains constant for the next 5 seconds, after that it decrease in such a way that a value equal to zero is reached at the 15 second. Since that time, all the components of the angular velocity reference of the testbed remain null. The desired angular velocities are $\omega = [7,3,1]^T$ deg/s. The reference signals for the vectorial part of the quaternion have been suitably calculated utilizing the angular velocity reference signals. The simulation time step and the control laws sample time is 25 ms. The Euler's method `ode4` was used to solve the differential equations.

3.4.1 STW results

The first simulation has been performed implementing the STW sliding mode (3.29). The following figures show the evolution of the state vector components and other relevant parameters during the manoeuvre. The gains used in the simulations are reported in Table 3.1:

Gain	Numerical value
k_1	0.1
k_2	1
α	0.01

Table 3.1. STW parameters

In Fig. 3.6 the angular velocity in body axis is reported. Fig. 3.5 shows the vectorial part of the quaternion which indicates the attitude of the testbed. Fig. 3.12 shows the variation over time of the gimbal angles. Except for the gimbal angle for which no reference signal is explicitly specified, the actual state overlaps perfectly the reference vector with the exception of small fluctuations when the slope of the reference quantity changes.

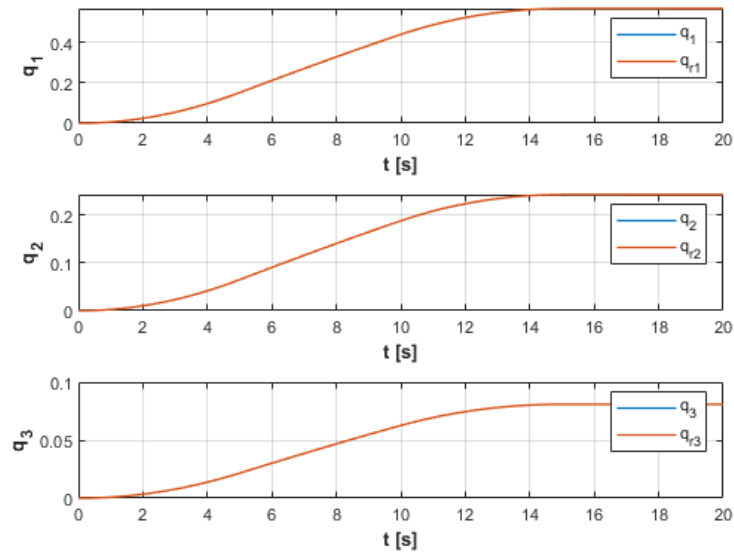


Figure 3.5. Vectorial part of quaternion (STW)

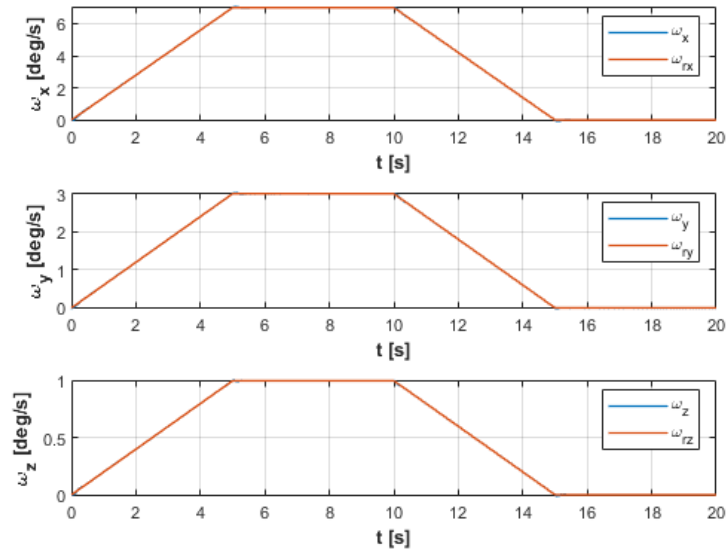


Figure 3.6. Angular velocity of testbed (STW)

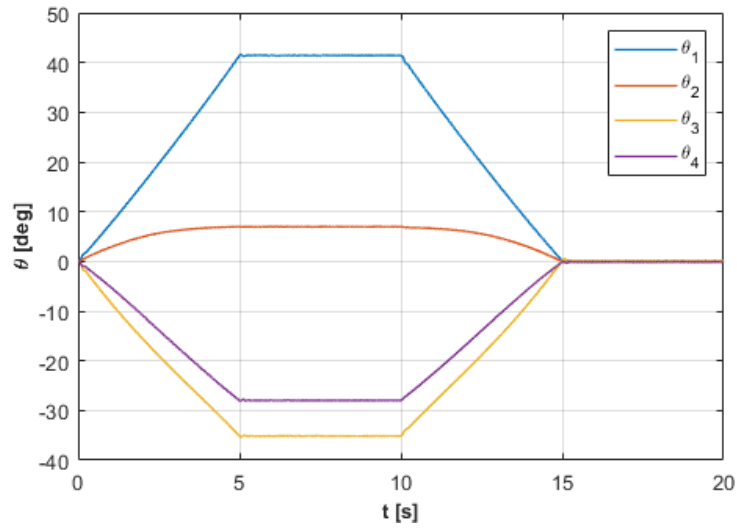


Figure 3.7. Gimbal angles (STW)

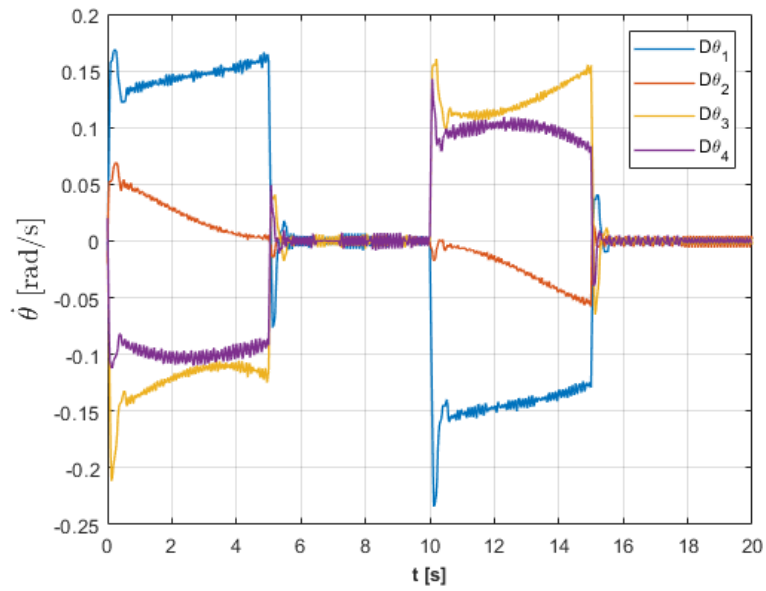


Figure 3.8. Gimbal rates (STW)

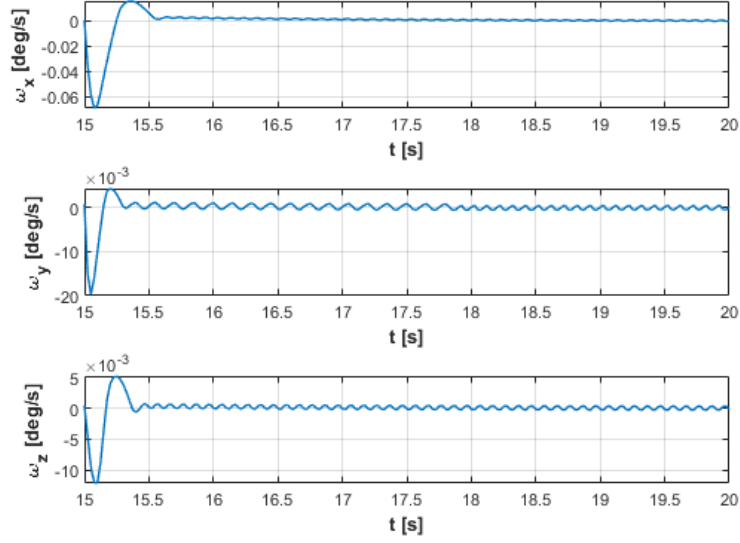


Figure 3.9. Angular velocities steady-state error (STW)

3.4.2 ACTW results

The same manoeuvre was performed with the ACTW controller. In this case more parameters have to be defined in order to comply to Equations 3.30 - 3.33.

Parameters	Numerical value
k_1	$8 \cdot 10^{-4}$
k_2	$7 \cdot 10^{-2}$
k_3	10^{-3}
k_4	1
tol	10^{-3}
l	10
L_{max}	4
L_{min}	0.5
τ	8

Table 3.2. ACTW parameters

Results of Figures 3.10 - 3.11 - 3.12 are quite similar to the ones obtained with STW (Fig. 3.5 - 3.6 - 3.7) but, we can see an higher fluctuation in Figure 3.11 (ω_z) with respect to Figure 3.6. Then, the control inputs are shown in Figures 3.8 and 3.13.

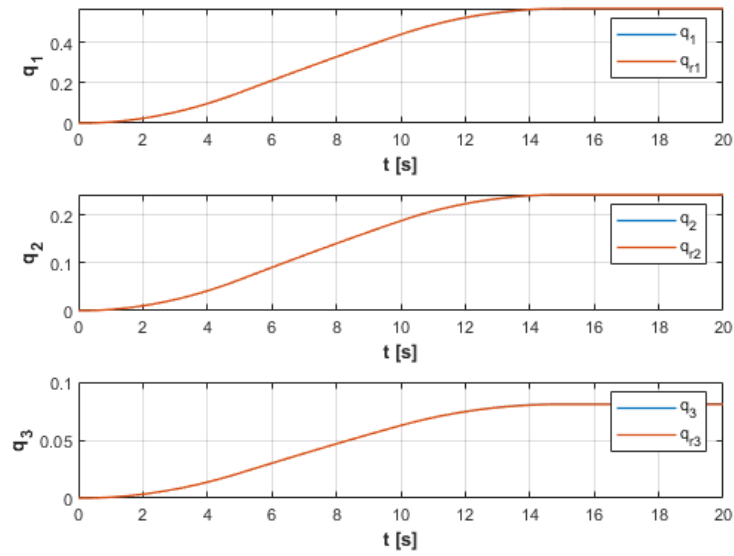


Figure 3.10. Vectorial part of quaternion (ACTW)

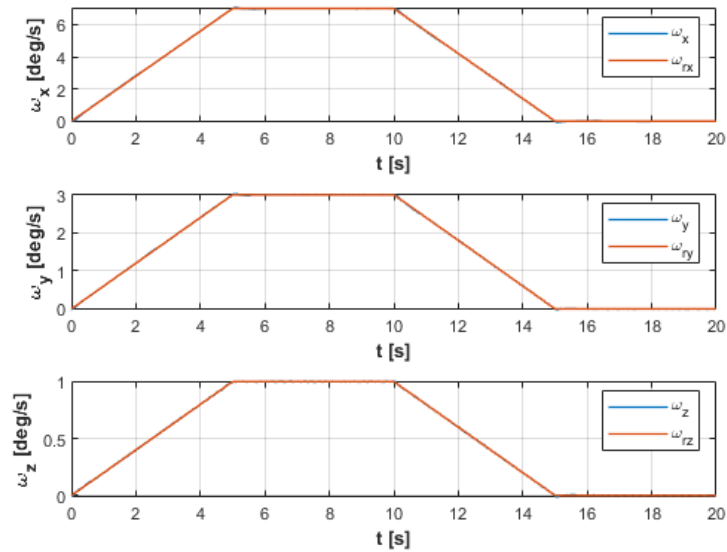


Figure 3.11. Angular velocity of testbed (ACTW)

The gimbal rates applied by the STW SMC is smaller, so a lower control authority is required by the STW. As deeply explained in [43], considering the controller

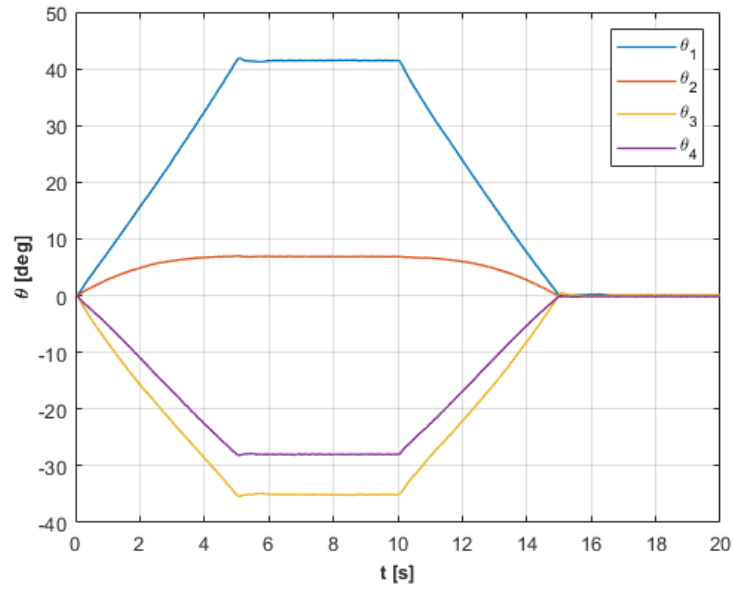


Figure 3.12. Gimbal angles (ACTW)

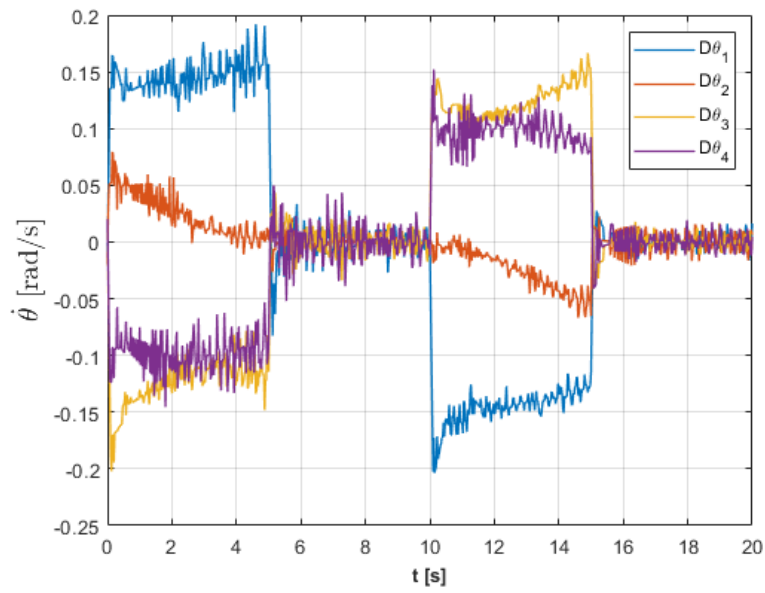


Figure 3.13. Gimbal rates (ACTW)

sample time Δt_{con} , the accuracy of the steady state error can be evaluated as $O(\Delta t_{con}^3)$ for \tilde{q} , and $O(\Delta t_{con}^2)$ for ω_{err} . Since the time histories of the quaternion

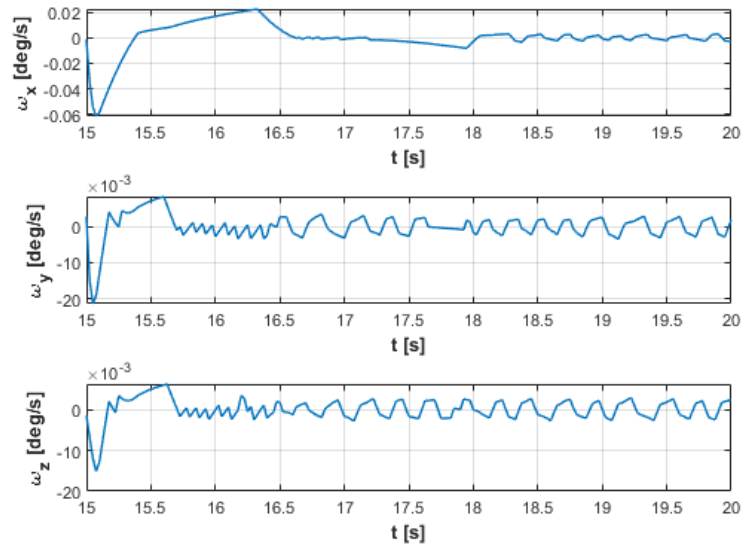


Figure 3.14. Angular velocities steady-state error (ACTW)

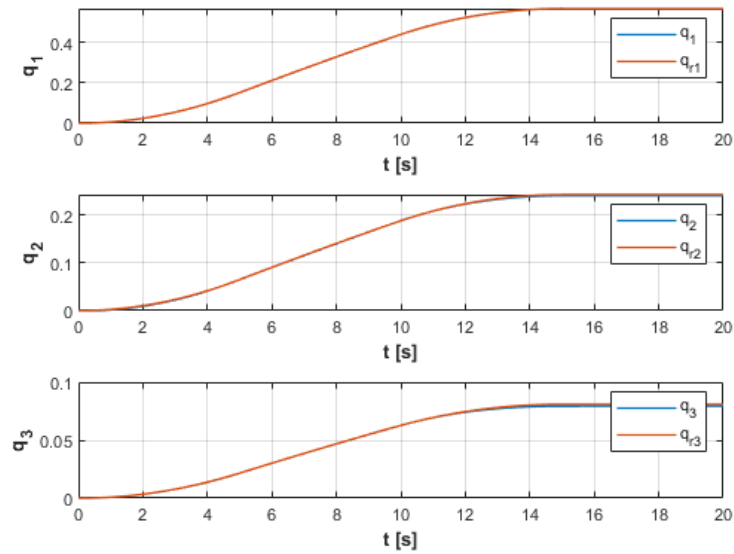


Figure 3.15. Vectorial part of quaternion (ACTW) when an higher disturbance is applied

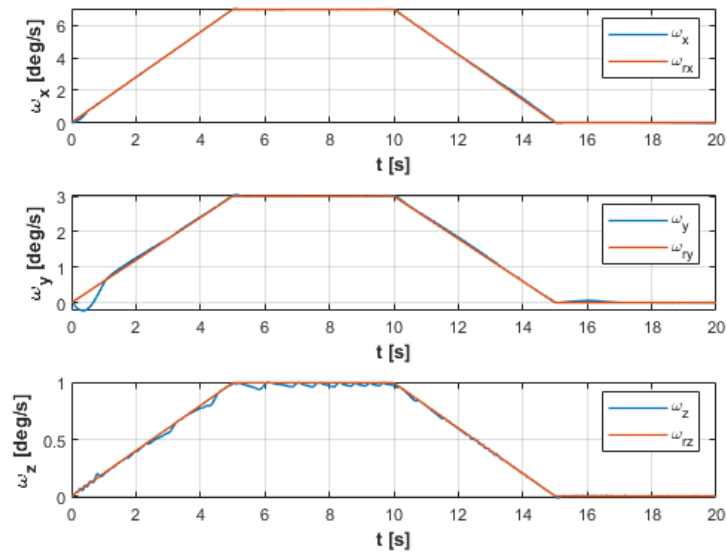


Figure 3.16. Angular velocity of testbed (ACTW) when an higher disturbance is applied

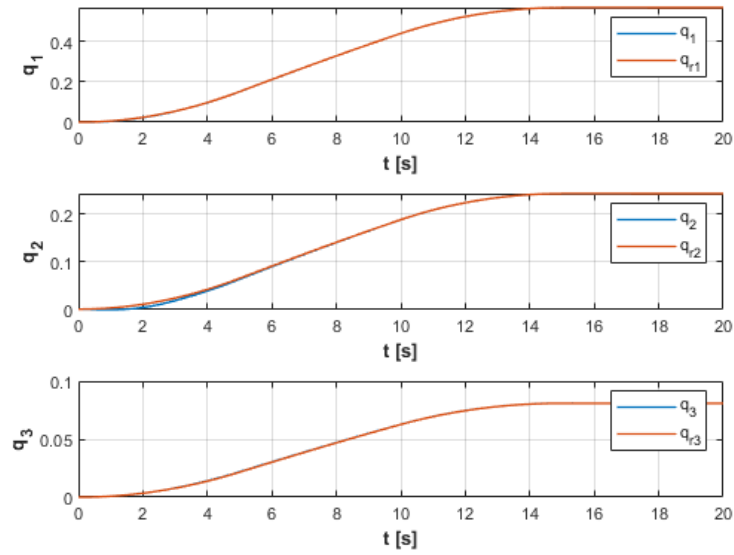


Figure 3.17. Vectorial part of quaternion (STW) when an higher disturbance is applied

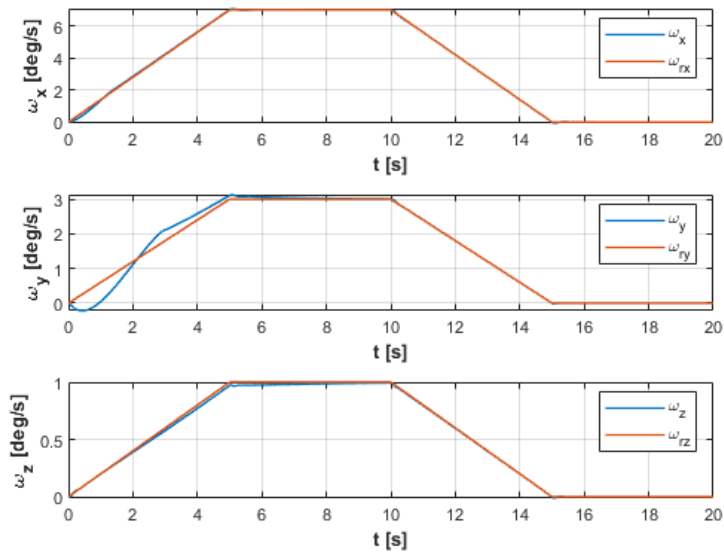


Figure 3.18. Angular velocity of testbed (STW) when an higher disturbance is applied

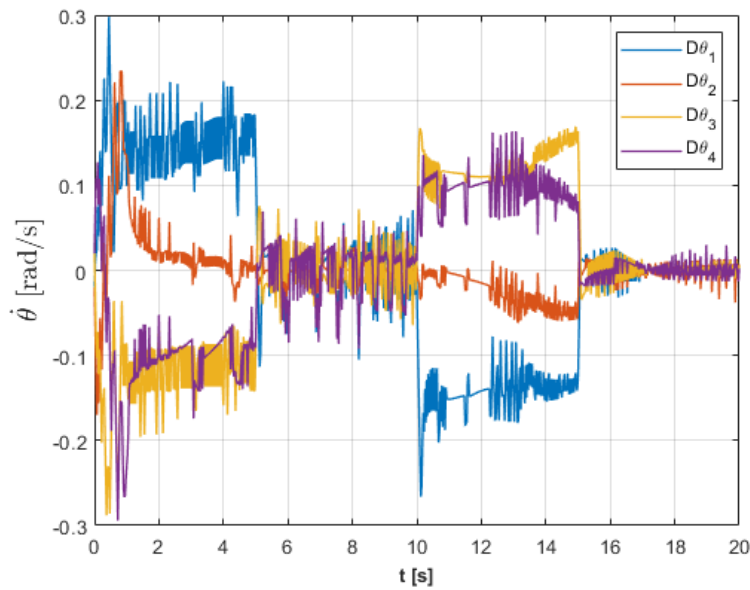


Figure 3.19. Gimbal rates (ACTW) when an higher disturbance is applied

vector are similar for both controllers, the tracking error is about 10^{-5} , which is lower than $19\Delta T_{con}^3 = 2.97 \cdot 10^{-4}$, as in [43]. Instead, an oscillatory behaviour of

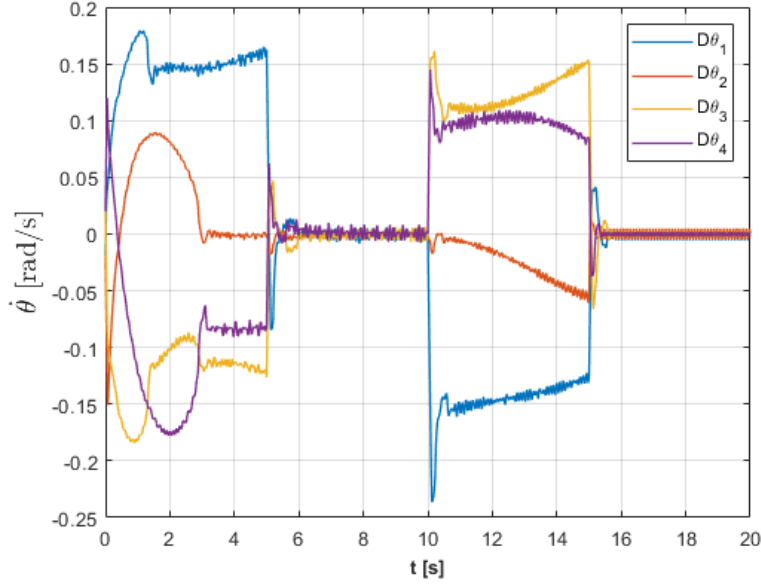


Figure 3.20. Gimbal rates (STW) when an higher disturbance is applied

the steady-state error for the angular velocities is observed in Figure 3.9, showing the residual chattering. The use of smoothing techniques may mitigate, or even eliminate, the residual chattering. In Figure 3.14, the residual chattering is less observable, even if the residual error is about one order of magnitude greater than in the STW SMC case. However, in both cases, $|\omega_e| \leq 19\Delta T_{con}^2 = 0.012 \text{ rad/s}$. The STW algorithm shows slightly better performance but it has a lower operating range with respect to the ACTW because the last one can change its gains adapting itself to environmental changes and disturbances.

A second scenario is considered to show the performance of these two controllers, when an external disturbances due to gravity torque 10 times greater is applied. Figure 3.18 shows how STW cannot track the angular velocity reference at the beginning of manoeuvre, in contrast to ACTW in Fig. 3.16 that can track the reference immediately changing its gains. We have to change the gains to adapt the STW controller. Instead, the disturbance is not affecting the performance of both controllers in terms of quaternion time history (see Figures 3.17 and 3.15). Finally, in Figure 3.19 is shown the control input of ACTW SMC when an higher disturbance is applied. We can see an higher control authority because of the increased of gains.

Chapter 4

Attitude and position dynamics of a flexible spacecraft

In the last decades, the growth of space science technology has led to a development of spacecraft structures in order to meet some requirements for pointing precision, support for large solar panel and lighter structures to contain launch costs.

The approximation of rigid body doesn't always bring accurate results because spacecraft is often composed by some flexible appendages such as solar panels or lightweight structures. Performing an attitude maneuvering or the effect of external disturbances will lead to a continuous vibration of flexible appendages that will interfere with the attitude control [39]. When the flexible appendages are taken into account, attitude control will be very difficult to design, because its development necessarily involves a dynamic simulation of the vehicle being controlled and this is complicated. The equations of motion of a continuous mechanical system are partial differential equations and in the following chapter, this theme will be treated through a coordinate transformation. This coordinate are uncoupled so, each one is associated with a motion in which the entire vehicle participates. Coordinates that correspond to motion of more than one flexible or rigid body of the system are called *distributed* or *modal coordinates*. The equation of motion are independent, so the vehicle can undergo motion in which only one of the scalar coordinates of the system participates. In this mode of motion, all points of the vehicle oscillate at the same frequency (the normal-mode frequency) and the vehicle deforms periodically into the same deformed shape (the normal-mode shape). Each modal coordinate defines the response in the corresponding mode. The independence of these coordinates allows the independent calculation of their participation in the vehicle motion. This is the normal coordinate approach, it permits to judge which coordinates are so significant keep, and which may be neglected in coordinate truncation [29].

The purpose of this chapter is to analyze the attitude dynamics of a satellite which is driven by the same CMGs actuators used on the testbed and the ACTW SMC

attitude controller explained in Section 3.3.

4.1 Flexible spacecraft attitude model

The flexible spacecraft is composed of a rigid body and some flexible appendages. Its attitude can be described by two sets of equations: the kinematic equation and the dynamical equation. The kinematics of the spacecraft describes the attitude of the main body, it was explained in Section 2.2.4.

$$\dot{\mathbf{q}} = \frac{1}{2}\mathbf{\Gamma}(q)\boldsymbol{\omega}$$

The dynamical equation describes both the total rigid body motion and essential motions of flexible appendages. The following equation describes what has been said [29, 21, 39]:

$$\mathbf{J}\dot{\boldsymbol{\omega}} + \boldsymbol{\delta}^T \ddot{\boldsymbol{\eta}} = -\boldsymbol{\omega} \times (\mathbf{J}\boldsymbol{\omega} + \boldsymbol{\delta}^T \dot{\boldsymbol{\eta}}) + \mathbf{u} + \mathbf{D}(t) \quad (4.1)$$

As we can see, equation 4.1 is similar to the standard Euler's equation (2.13) but there are two terms proportional to $\boldsymbol{\delta}$ that represents the coupling matrix between the elastic and rigid structures. To calculate its components a modal analysis of flexible body has to be performed in order to elaborate the shape modes, their frequency and the corresponding eigenvectors which indicates the dynamic response of the system. $\boldsymbol{\delta}$ can be calculated as explained in [29]:

$$\boldsymbol{\delta} = -\boldsymbol{\phi}^T \mathbf{M}(\boldsymbol{\Sigma}_{0I} - \boldsymbol{\Sigma}_{I0} \tilde{\mathbf{R}} - \tilde{\mathbf{r}} \boldsymbol{\Sigma}_{I0}) \quad (4.2)$$

$\boldsymbol{\phi} \in \mathbb{R}^{6n \times m}$ is a matrix containing the eigenvectors, where n is the number of sub-bodies of the flexible appendage considered (Cap. 4.1.1) and m is the number of modes considered, in this case we look at the first two flexional modes and the first torsional one. $\mathbf{M} \in \mathbb{R}^{6n \times 6n}$ is the generalized inertia matrix of cantilevered appendage (see appendix B). $\mathbf{R} \in \mathbb{R}^3$ is a vector from an arbitrary point O fixed on the rigid part of the spacecraft and a point Q on the interface between the fixed body A and appendage B . $\mathbf{r} \in \mathbb{R}^3$ is the vector from Q to the center of mass of the sub-body P as shown in Figure 4.1. The \sim operator is explained in Appendix B. Moreover, there are two terms in Eq. (4.1) that have not been explained yet: \mathbf{u} is the control input, $\boldsymbol{\eta}$ is the modal coordinate vector and it can be calculated by solving the following dynamical system:

$$\ddot{\boldsymbol{\eta}} + \mathbf{C}\dot{\boldsymbol{\eta}} + \mathbf{K}\boldsymbol{\eta} = -\boldsymbol{\delta}\dot{\boldsymbol{\omega}} \quad (4.3)$$

Equation (4.3) describes the flexible dynamics, under the assumption of small deformation. As we can see, the right member in Eq. (4.3) is proportional to the angular acceleration, thus the disturbance due to flexibility is related to the magnitude of $\dot{\boldsymbol{\omega}}$. This means that external disturbances and control inputs generate a

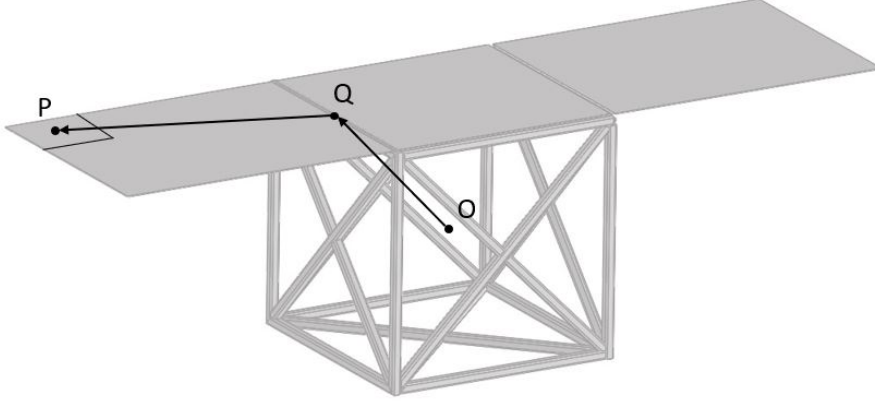


Figure 4.1. Discrete-parameter appendage sub-body coordinates

reaction torque by the flexible appendage. Therefore, $\mathbf{C} = \text{diag}[2\xi_i\omega_{ni}, i = 1, \dots, N]$ is a damping (diagonal) matrix, $\mathbf{K} = \text{diag}[\omega_{ni}^2, i = 1, \dots, N]$ is a stiffness matrix, N is the number of mode taken into account, ω_n , ξ are the natural frequency and the corresponding damping, respectively. There may be some errors when measuring or estimating the inertia matrix \mathbf{J} , coupling matrix $\boldsymbol{\delta}$, \mathbf{C} , and \mathbf{K} . Under these circumstances, a term $\mathbf{D}(t)$ is added to take into account external disturbance torques and possible variations with respect to the nominal values of parameters. There exists a positive constant D such that:

$$\|\mathbf{D}(t)\| \leq D \quad (4.4)$$

4.1.1 Sub-bodies division and modal analysis

In what follows, attention is focused first upon an individual flexible appendage. The appendage A attached to a primary rigid base B . Deformations due to flexibility are felt in changing the attitude of the primary base. For convenience in derivation and for compatibility with engineering practice, the flexible appendage A is idealized initially as a collection of elastically interconnected, discrete rigid sub-bodies A_1, A_2, A_N [29]. The sub-bodies are undergoing small deformations while rotating in an arbitrary way relative to the rigid part of the spacecraft subject to any translation and rotation. Damping mechanisms are excluded from this idealization, but modal damping is incorporated in the equations at a later stage of the derivation, with the introduction of modal coordinates for the appendage, as deeply explained in [29]. We consider a cube $520 \times 520 \times 520 \text{mm}$ (dimension chosen to contain the testbed actuators) spacecraft with an aluminium truss chassis. Solar panels are arranged as in Figure 4.2 and their dimensions are $500 \times 625 \times 3 \text{mm}$. As a consequence vector \mathbf{r} can be calculated. Last term of Eq. (4.2) is $\boldsymbol{\phi}$ so, a

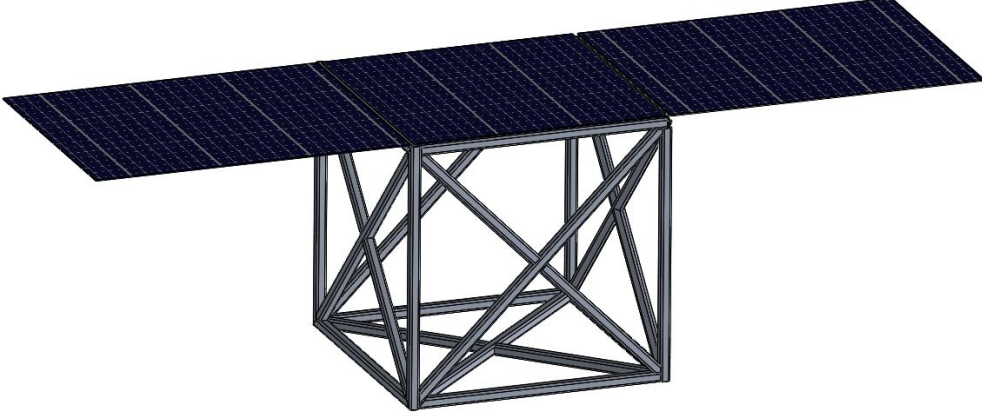


Figure 4.2. Spacecraft CAD model

modal analysis is necessary to calculate eigenvectors and system modal frequency. In order to compute this analysis, we need to solve a particular case of the ordinary dynamic system. In general, the equations of motion can be expressed as a function of the system mass, stiffness, damping and applied loads like in Eq. (3.1):

$$[M]\ddot{x}(t) + [C]\dot{x}(t) + [K]x(t) = P(t) \quad (4.5)$$

where M is the global mass matrix, K is the global stiffness matrix, C is the global damping matrix and P is the global load vector. Eigenvalues or natural frequencies are found when there is no damping or applied loads. The equations of motion for free vibration can then be written as:

$$[M]\ddot{x}(t) + [K]x(t) = 0 \quad (4.6)$$

To solve this differential equation, a sinusoidal solution is imposed:

$$x(t) = \phi e^{i\omega t}$$

As a consequence the expression of $\ddot{x}(t)$ is:

$$\ddot{x}(t) = -\omega^2 \phi e^{i\omega t}$$

By replacing the above equalities into Eq. (4.6), the equation of motion becomes:

$$(-\omega^2[M] + [K])[\phi]e^{i\omega t} = 0 \quad (4.7)$$

Since $e^{-i\omega t}$ is never zero, it can be divided mathematically and the equation can be rearranged into an eigenvalue problem as in [35]:

$$([K] - \lambda[M])[\phi] = 0 \quad (4.8)$$

in which ϕ is the eigenvector for each mode that represents the natural mode shape; λ is the eigenvalue for each mode and it is related to system's natural frequency: $\lambda_i = \omega_i^2$ in which ω is the natural frequency that is used to calculate the matrix C and K in Eq. (4.3) [35].

To solve the problem (4.8), FEM (Finite element method) softwares was used: the pre-processor *Patran* and the solver *Nastran*.

4.2 Position dynamics and control

The first step is to understand the fundamental laws that describe the relative position dynamics between two spacecrafts, a chaser and a target. For the analysis of rendezvous trajectories, it is best to use a reference frame originating in the center of mass of the target vehicle. This frame is the spacecraft local orbital frame of the target, defined in Section 2.1.3. If the following assumptions are met, the *Hill's equations* are an accurate approximation of the relative motion:

- The orbits are circular and in LEO;
- The validity of the approximation of Hill's equations is limited to few kilometers of distance along each axes ($\sim 10km$);
- The target moves under the influence of a central gravity field only;
- The chaser moves under the influence of: external disturbances and actuation system

Therefore, the Hill's equation can be written:

$$\begin{aligned} \ddot{x} &= 2\omega\dot{z} + \frac{1}{m_c}F_x \\ \ddot{y} &= -\omega^2y + \frac{1}{m_c}F_y \\ \ddot{z} &= -2\omega\dot{x} + 3\omega^2z + \frac{1}{m_c}F_z \end{aligned} \quad (4.9)$$

ω is the angular velocity of the orbit related to the target and can be calculated as $\omega = \sqrt{\frac{\mu}{r^3}}$ where $\mu = 398600 km^3s^{-2}$ is the *gravitational parameter* for the Earth and r is the radius vector from the Earth's center to the target. m_c is the mass of chaser and it varies because the fuel mass decrease performing manoeuvre according to [9]. $F = [F_x F_y F_z] \in \mathbb{R}^3$ is the total force vector, which is the sum of the forces due to

the thrusters and the actions of the external environment disturbances affecting the system. The force due to the thrusters is assumed to be affected by errors because of the uncertainties in the shoot and magnitude of the thrusters. The vector of forces obtained from the thrusters is converted from the body reference frame to the *LVLH* frame through the following relation:

$$F = L_{IB}^* F^*$$

in which $F^* \in \mathbb{R}^3$ is the force vector expressed in the body frame, $F \in \mathbb{R}^3$ is the one in the *LVLH* reference system and L_{IB} is the rotation matrix between two reference frames [15].

4.2.1 Position actuator model

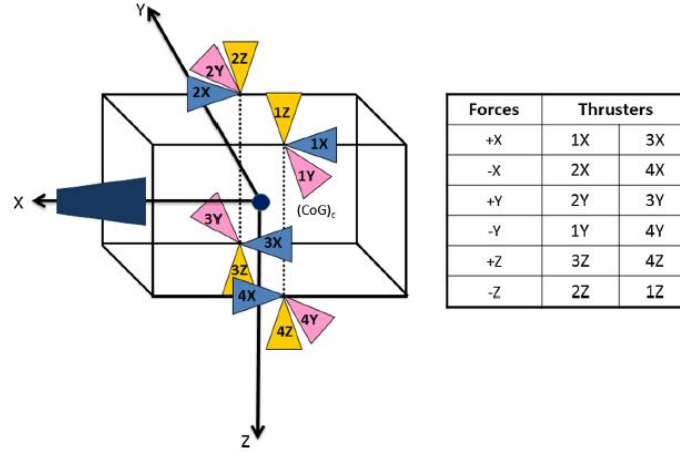


Figure 4.3. Thruster scheme on the spacecraft [15]

The actuation system is composed of 12 thrusters (see Fig. 4.3). They translate the on/off command computed by the controller into thrust and moment variations, according to their shoot direction and their location with respect to the center of mass (CoM) position, and they cannot be modulated. A zero nominal moment is ensured with the definition of thrusters position as in Fig. 4.3 [15]. The magnitude of the force applied by the i_{th} thruster is modeled as

$$T_{mag_i} = T_{max} + \Delta T_{mag_i} \quad (4.10)$$

In which $T_{max} \in \mathbb{R}$ is the maximum force that can be produced by each thruster, $\Delta T_{mag_i} \in \mathbb{R}$ is a random error in the magnitude of the force applied by i_{th} thruster components as in [48, 49].

4.2.2 H_∞ position controller

Differently from attitude dynamics, an H_∞ is chosen to control the position dynamics. In Eq. (3.3) the classic dynamic system was introduced but, generally, it is more complicated. For example, considering the Figure 4.4, there are two inputs in the plant: u and w . u is the control command while w represents jamming signals. The main characteristic of this controller is to minimize the maximal gain between input disturbances and the frequency response of the system, so if there are some disturbances, they must interfere as little as possible with what we are interested in.

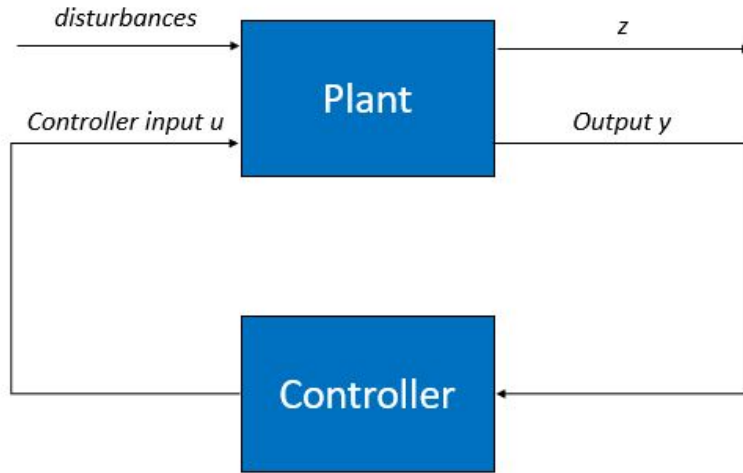


Figure 4.4. System scheme

The H_∞ norm of a proper LTI system from input $w(t)$ to output $z(t)$, is the induced energy-to-energy gain (induced L_2 norm, see Appendix C) defined as [38, 52]:

$$\|G(j\omega)\|_\infty = \sup_{\omega \in \mathbb{R}} \bar{\sigma}(G(j\omega)) = \sup_{w(s) \in H_2} \frac{\|z(s)\|_2}{\|d(s)\|_2} = \max_{w(t) \in L_2} \frac{\|z\|_2}{\|w\|_2} \quad (4.11)$$

For a SISO systems, it represents the maximal peak value on the Bode diagram of $G(j\omega)$, that is the largest gain if the input is harmonic. For a MIMO system, it is the maximum singular value. Differently from H_2 norm, the H_∞ norm cannot be computed analytically, only numerical solutions can be obtained.

The H_∞ norm can be computed using an LMI (Linear matrix inequality) way (see ??). The L_2 norm of the output z of a system LTI is uniformly bounded by γ times the L_2 norm of the input w . A dynamical system $G = (A, B, C, D)$ where:

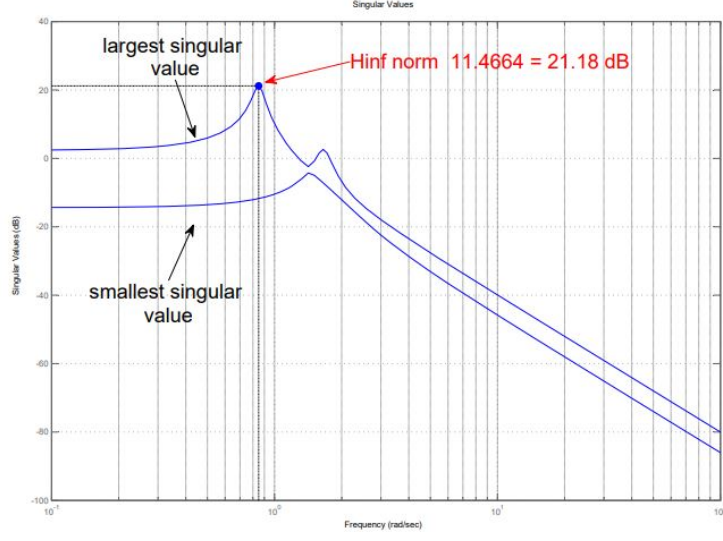


Figure 4.5. Bode diagram [38] (pp 11)

$$\begin{aligned} \dot{x} &= Ax + Bu \\ y &= Cx + Du \end{aligned} \quad (4.12)$$

is internally stable with $\|G\|_\infty < \gamma$ if there exists a positive definite symmetric matrix $P = P^T > 0$ satisfying:

$$\begin{bmatrix} A^T P + PA & PB & C^T \\ B^T P & -\gamma I & D^T \\ C & D & -\gamma I \end{bmatrix} < 0 \quad (4.13)$$

And the resulting controller is given by:

$$K = B^T P \quad (4.14)$$

Controller design

In this section, we will investigate the control problem of spacecraft rendezvous with a noncooperative target. The purpose of H_∞ is to find the following controller:

$$u = Kx \quad (4.15)$$

where K is a constant feedback control gain to be determined with Eq. (4.14). The controller K , which based on the information in y , generates a control signal u that contrast the influence of w on z , thus minimizing the closed-loop norm from w to z .

Considering the set of equations (4.12) and keeping in mind that the principal aim is to solve the LMI (4.13), we need to find the matrix A , B , C , D that compose the systems (4.12). In order to do this, considering the Hill's equation written previously in Eq. (4.9), the vector x can be written as a six dimension array in which the components are the position and the velocity in a *LVLH* frame centered on the target. Therefore, the matrix can be written as:

$$x = \begin{bmatrix} x \\ y \\ z \\ \dot{x} \\ \dot{y} \\ \dot{z} \end{bmatrix}; \quad A = \begin{bmatrix} 0 & 0 & 0 & 1 & 0 & 0 \\ 0 & 0 & 0 & 0 & 1 & 0 \\ 0 & 0 & 0 & 0 & 0 & 1 \\ 0 & 0 & 0 & 0 & 0 & 2\omega \\ 0 & -\omega^2 & 0 & 0 & 0 & 0 \\ 0 & 0 & 3\omega^2 & -2\omega & 0 & 0 \end{bmatrix}; \quad B = \frac{1}{m} \begin{bmatrix} 0 & 0 & 0 \\ 0 & 0 & 0 \\ 0 & 0 & 0 \\ 1 & 0 & 0 \\ 0 & 1 & 0 \\ 0 & 0 & 1 \end{bmatrix} \quad (4.16)$$

The output vector y has to be chosen in order to have a quantity to track by the controller. The state vector $[x, y, z]$ has been chosen:

$$y = \begin{bmatrix} x \\ y \\ z \end{bmatrix}; \quad C = \begin{bmatrix} 1 & 0 & 0 & 0 & 0 & 0 \\ 0 & 1 & 0 & 0 & 0 & 0 \\ 0 & 0 & 1 & 0 & 0 & 0 \end{bmatrix} \quad (4.17)$$

D is the null matrix in order to verify the equality (4.12).

4.3 Orbital manoeuvres

In chapter 1, the rendezvous manoeuvre was introduced: it is the set of operations during which a spacecraft chaser conducts a set of operations to reach a location closer to another satellite called target. In this work two steps of the complete rendezvous manoeuvre are analyzed: the Hohmann transfer and the Radial boost. The first one has the purpose to ensure that the chaser reaches the same altitude, so the same target orbit; in the second one the chaser reduces the longitudinal distance between the two bodies, and often there are many radial boost to make more verifications of the position in order to improve the security of the entire process. After all, there are the close approach in which the chaser can reach the docking or berthing condition.

The discussion of orbit manoeuvre in this section assumes that all manoeuvres are impulsive. They consist of an instantaneous change of velocity at the point where the manoeuvre is applied. This is a first approximation, which makes the problem easier to explain the effects on a large scale [19].

4.3.1 Hohmann transfer

The Hohmann transfer is an impulsive manoeuvre from a lower to an higher circular orbit or vice versa by two tangential boosts, separated by half an orbital revolution [19]. The Hohmann transfer is the most efficient two-impulse manoeuvre for transferring between two co-planar circular orbits. The first impulse ΔV_{x1} is tangential in order to improve the energy of the orbit. This action increase the orbit dimension and transform it in an elliptic transfer orbit which has the perigee on the first orbit and the apogee on the second one. When the chaser reaches the apogee, a second tangential impulse ΔV_{x2} is performed in the same direction of the motion in order to increase the energy and circularize the orbit. A graphic representation is reported in Figure 4.6.

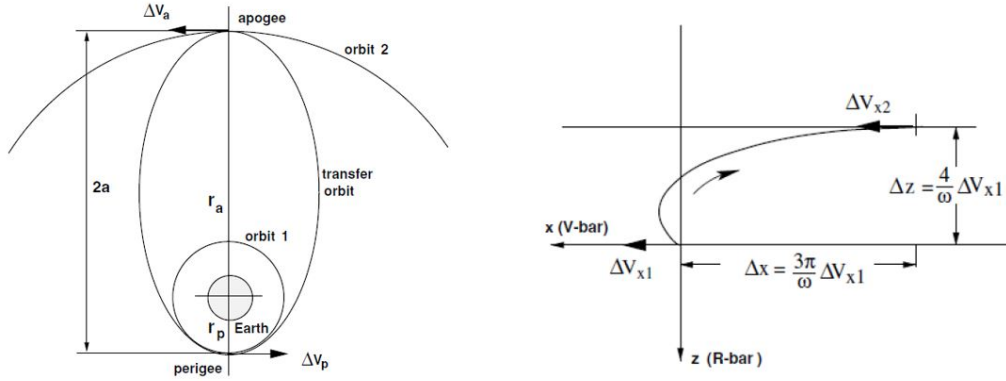


Figure 4.6. Hohmann transfer: inertial frame on the left, *LVLH* frame on the right [19](pp 38-52)

The two impulses are calculated by the following equation in a *LVLH* frame:

$$\Delta V_{x1} = \Delta V_{x2} = \frac{\omega}{4} \Delta z \quad (4.18)$$

in which Δz is the altitude difference between the two bodies and ω is the angular velocity of the target.

4.3.2 Radial boost

The Radial boost is a radial manoeuvre where the impulses transfer are along V-bar (2.1.3). As deeply explained in [19], a particular property of radial manoeuvres is that they affect only the eccentricity, not the orbital period, and thus cause no drift with respect to the target orbit. Figure 4.7 shows the application of ΔV in radial direction: the radial boost starts at a position x_1 on the target orbit to reach a

position x_2 closer to the target. To stop the motion at x_2 , an impulse of the same magnitude and direction, $\Delta V_{z1} = \Delta V_{z2}$ must be applied:

$$\Delta V_{z1} = \Delta V_{z2} = \frac{\omega}{4}(x_2 - x_1) \quad (4.19)$$

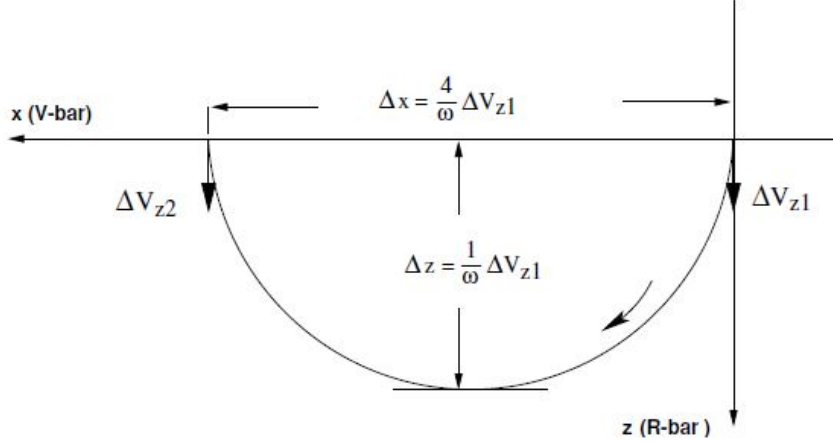


Figure 4.7. Transfer along V-bar by radial impulses [19] (pp 55).

4.4 Orbital disturbances

The most significant disturbances depend on the class of orbit in which the rendezvous manoeuvre is performed. For example, in a LEO (as happens in this work) the most significant disturbance is the drag due to residual atmosphere. On the other hand in GEO the most significant disturbance is the solar radiation pressure. Other disturbances are due to magnetic field, gravitational field and geopotential anomaly due to the shape of the Earth that deviates from an ideal sphere. Large uncertainties remains for the disturbances due to the limited knowledge on these phenomena and modeling errors of the spacecraft surfaces [19]. The purpose of this section is to provide an overview of the orbital disturbances taken into account in the mathematical model of the system: the aerodynamic drag for the trajectory dynamics and the gravity gradient for the attitude.

4.4.1 Aerodynamic drag

In LEO there is still some residual atmosphere. However, the density is so low that we cannot apply conventional fluid mechanics theories based on continuum model. Instead, the interaction between the atmosphere and the spacecraft must be treated

at the molecular level. As in [5], in this discussion the following assumption are made:

- The momentum of molecules impacting on the surface is totally lost
- The thermal motion of the atmosphere is much smaller than the spacecraft speed
- The spacecraft is nominally non-spinning

The aerodynamic drag vector in body coordinates is given by [19]:

$$F_A = -\frac{1}{2}\rho S C_D V^2 \quad (4.20)$$

in which ρ is the atmosphere density, C_D is the drag coefficient and depend on the type of reflection of the incident molecules impacting the surface of the object. The vector is on the same direction of velocity but in the opposite side. The force is applied on the aerodynamic center of pressure and if it's not coincident with the center of mass, an aerodynamic torque is generated:

$$\mathbf{T}_A = \mathbf{r}_A \times \mathbf{F}_A \quad (4.21)$$

\mathbf{r}_A is the vector from the body center of mass to the aerodynamic center of pressure.

4.4.2 Gravity gradient

In space the gravitational field is not uniform, and the consequent variations in the specific gravitational force generate a torque around the center of mass of the body. If the gravitational field were uniform over a material body, then the center of mass become the center of gravity and the gravitational torque is null. In this discussion, we assume only one celestial primary body (the Earth) and it possesses a spherically symmetrical mass distribution. The main concept is expressed in Figure 4.8 related to the intensity of gravitational field, which decrease with r^2 , r is the distance between the Earth and spacecraft.

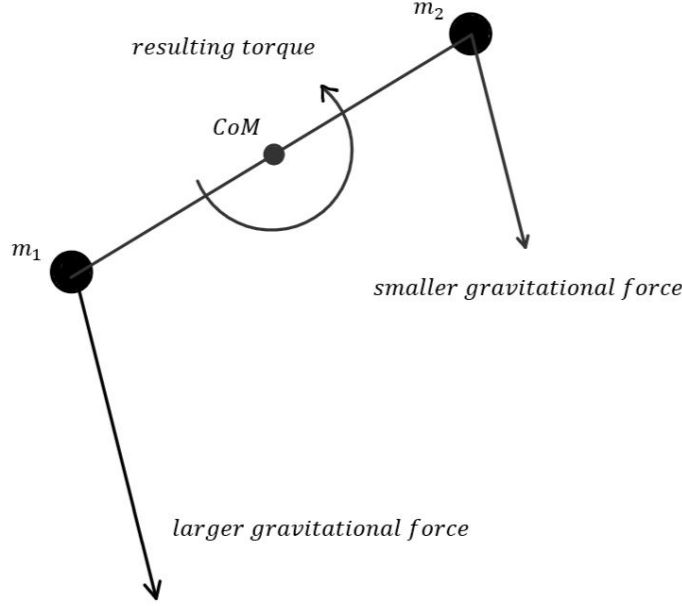


Figure 4.8. Gravity gradient effect [5]

The gravity gradient torque is given by [5]:

$$\mathbf{T}_G = 3n^2 \cdot \hat{r} \times \mathbf{J}\hat{r} \quad (4.22)$$

$n = \sqrt{\mu/a^3}$ is the orbital rate (a is the semi-axis of the orbit) and $\hat{r} = -r_{ECI}/\|r_{ECI}\|$, considering $r_{ECI} \in \mathbb{R}^3$ as the position of the spacecraft respect to the inertial frame.

4.5 Simulation environment and results

As in Section 2.3, a scheme of mathematical model is proposed in Fig. 4.9. The attitude model is the same, except for the attitude dynamics in which Eq. (4.1) and 4.3 were implemented. An ACTW SMC controller as in 3.31 is used. The position model operations starts from the Hill's equation. At an initial moment the two spacecrafts are moving on their orbits and the reference vector is the same as the output vector from the Hill's equation. When manoeuvre begins, the reference vector and the actual state are no longer equal so the navigation control block begins to work in order to track the reference. The control input enters in the Thruster modulator block where the thrusters dynamics is taken into account. Table 4.1 shows the physical properties of the flexible spacecraft.

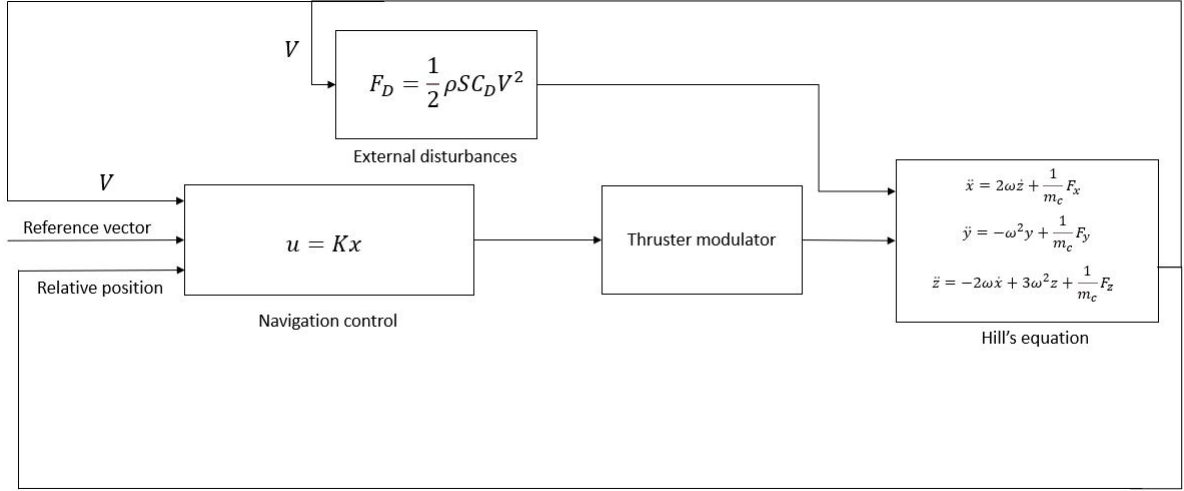


Figure 4.9. Simulink scheme

Variable	Nomenclature	Numerical value	Units
Mass of the spacecraft	m	15.1	kg
Inertia matrix	J	$\begin{bmatrix} 1.88 & 0 & 0 \\ 0 & 0.6882 & 0 \\ 0 & 0 & 1.811 \end{bmatrix}$	kg · m ²
Angular momentum of each wheel	h_ω	0.0576	kg m ² /s
Skew angle	β	45	deg

Table 4.1. Physical properties of the spacecraft

Parameters	Numerical value
k_1	$4 \cdot 10^{-3}$
k_2	$3 \cdot 10^{-2}$
k_3	$3 \cdot 10^{-5}$
k_4	$7 \cdot 10^{-4}$
tol	0.1
l	0.5
L_{max}	5
L_{min}	0.01
τ	10

Table 4.2. Attitude Controller parameters

The flexible properties were found after a modal analysis, they are:

$$\boldsymbol{\delta} = \begin{bmatrix} -0.0195 & 0 & 0 \\ 0 & 0.0024 & 0 \\ -0.0050 & 0 & 0 \end{bmatrix} kg^{\frac{1}{2}}m/s^2 \quad (4.23)$$

$$\omega_{n1} = 4.3434, \quad \omega_{n2} = 11.7521, \quad \omega_{n3} = 26.3946$$

This implies

$$\mathbf{K} = \text{diag}[18.8648, 138.1119, 696.6749], \quad \mathbf{C} = \text{diag}[0.1737, 0.4701, 1.0558]$$

ζ is assumed 0.02. The initial conditions of the chaser position are set to $[x_0, y_0, z_0]_{LVLH} = [-10, 0, 3] \cdot 10^3 m$ and the desired position at the end of manoeuvre is set to $[x, y, z]_{LVLH} = [-400, 0, 0] m$. A rotation manoeuvre is performed starting from a quaternion $q = [0.5, 0.5, 0.5, 0.5]$ to a final $q = [1, 0, 0, 0]$. The desired angular velocity is $\omega_{ref} = [0, 0, 0]$.

Fig. 4.10 shows the evolution of quaternions. The desired attitude is reached in less than 100 s. In figures, the first 1000 s are only shown in order to make more readable the figures because the rest of simulations have the same behaviour as the first seconds (the total duration is approximately 5500 s). Fig. 4.11 shows the evolution of the angular speed error of the spacecraft. The quaternions and angular rate errors at the end of the simulation are of the order of $\|q_{err}\| = 3.83 \cdot 10^{-6}$ and $\|\omega_{err}\| = 5.47 \cdot 10^{-5}$. These errors prove the good performance of ACTW controller. Controller increase the gains to reach the desired attitude ensuring to perform a fast manoeuvre. When the equilibrium point is reached, controller reduces the gains in order to have a fine control, as shown in Fig. 4.12 in which the evolution of the gain L is proposed. In Eq. (4.1) there are two contributions due to flexibility: $-\delta^T \ddot{\eta}$ and $-\omega \times \delta^T \dot{\eta}$ reported in Figures 4.13 and 4.14. The contributions are proportional to $\dot{\omega}$ so, we can see an higher torque due to flexibility manoeuvring, then, the torque falls to a maximum value of $2.6 \cdot 10^{-7}$. Figure 4.15 shows the time history of modal coordinate η .

The gravity gradient torque is shown in Figure 4.16. The gravity torque has its maximum value at the beginning of manoeuvre, when the spacecraft reaches the desired attitude, it is aligned with respect to the local vertical frame, then the gravity torque falls to zero.

The Hohmann transfer is the first step of the rendezvous manoeuvre, it starts at point $x_0 = [-10000, 0, 3000]_{LVLH} m$ of Fig. 4.17 and 4.18. At the end of the Hohmann transfer, the chaser reaches the target orbit and its position is $[-3000, 0, 0]_{LVLH} m$. Then, a Radial Boost is performed to reach the final position $[-500, 0, 0]_{LVLH} m$. In Fig. 4.19 forces due to position H_∞ are proposed. The sampling time of thrusters subsystem is set to 1 Hz.

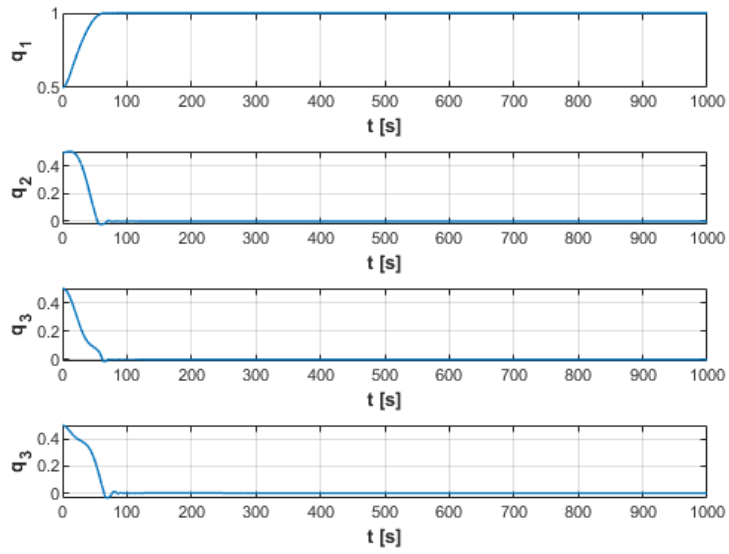


Figure 4.10. Vectorial part of quaternion

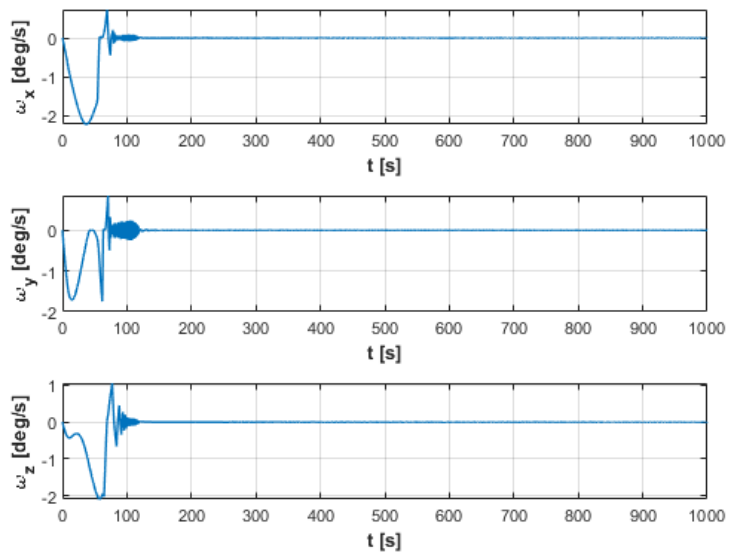


Figure 4.11. Variation of angular velocity of spacecraft

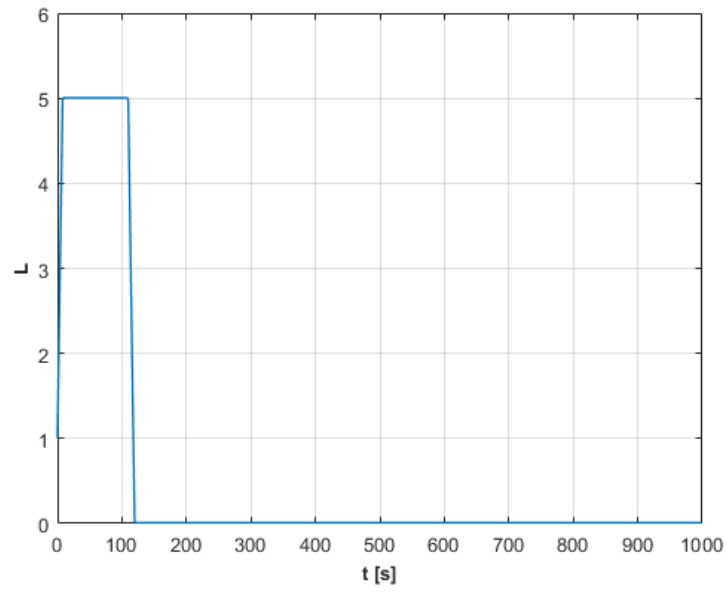


Figure 4.12. Time history of gain L

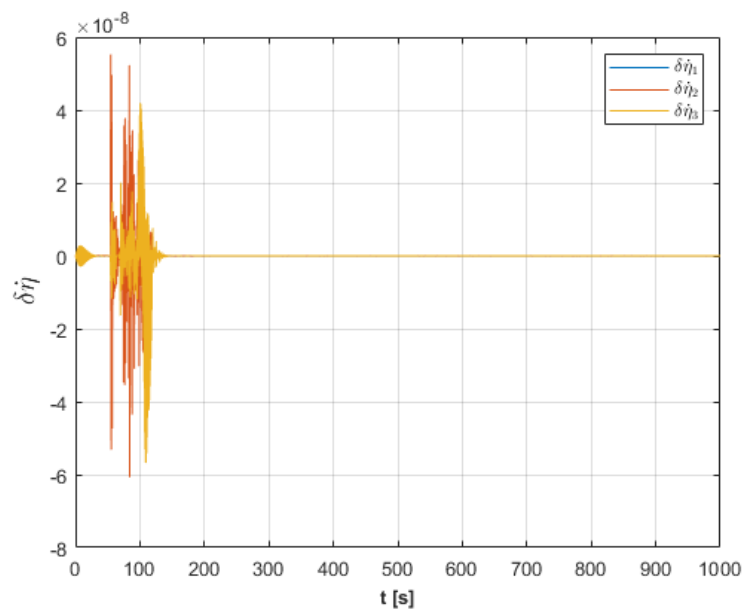


Figure 4.13. Time history of $\dot{\eta}$ contribution

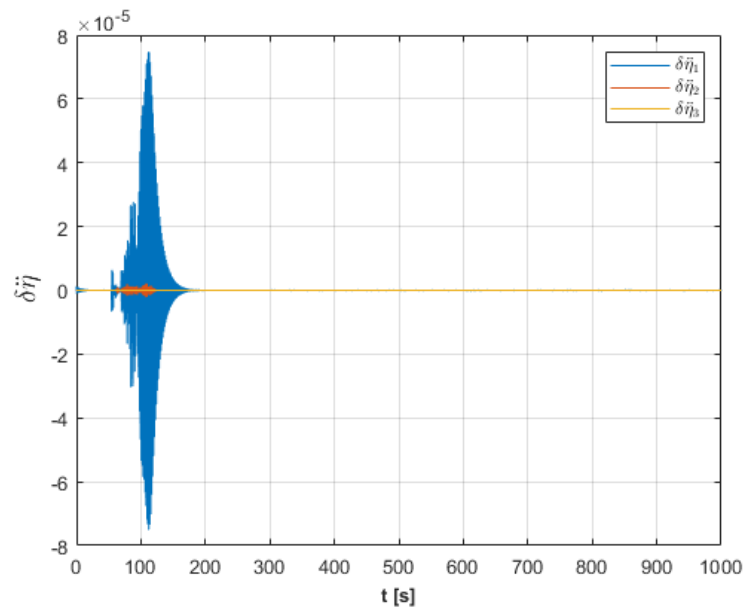


Figure 4.14. Time history of $\ddot{\eta}$ contribution

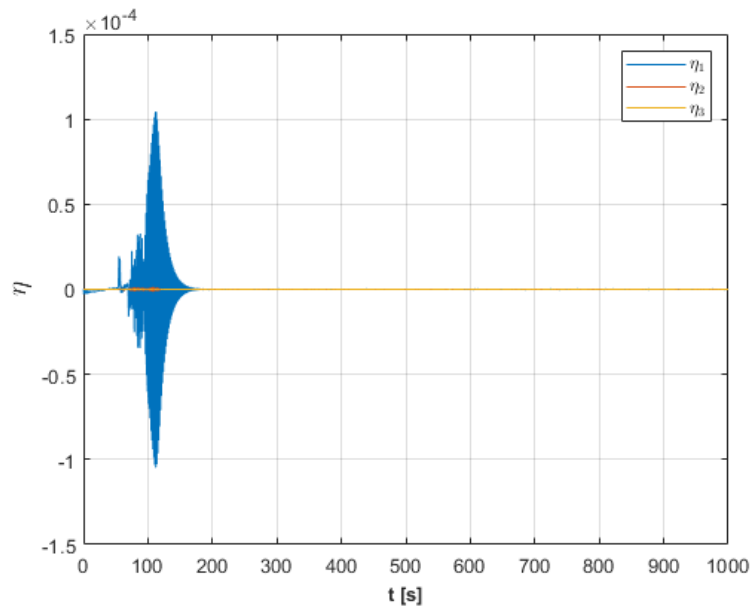


Figure 4.15. Time history of η

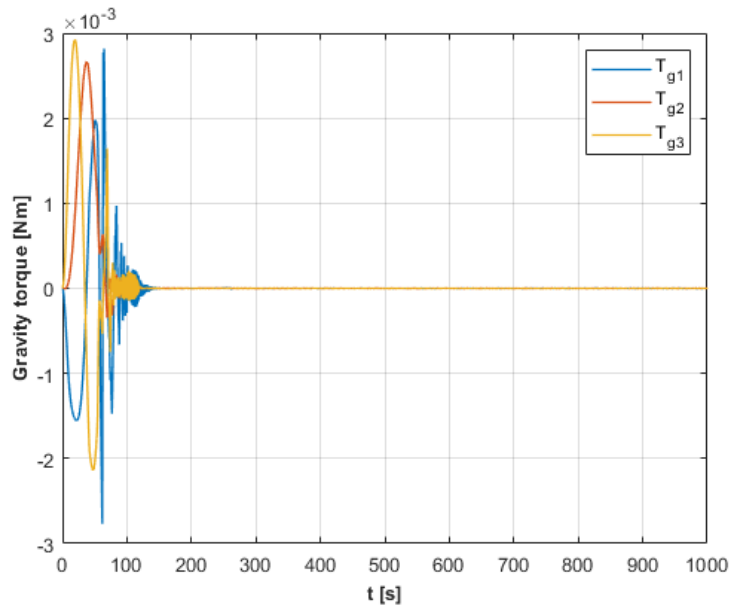


Figure 4.16. Time history of gravity gradient disturbance

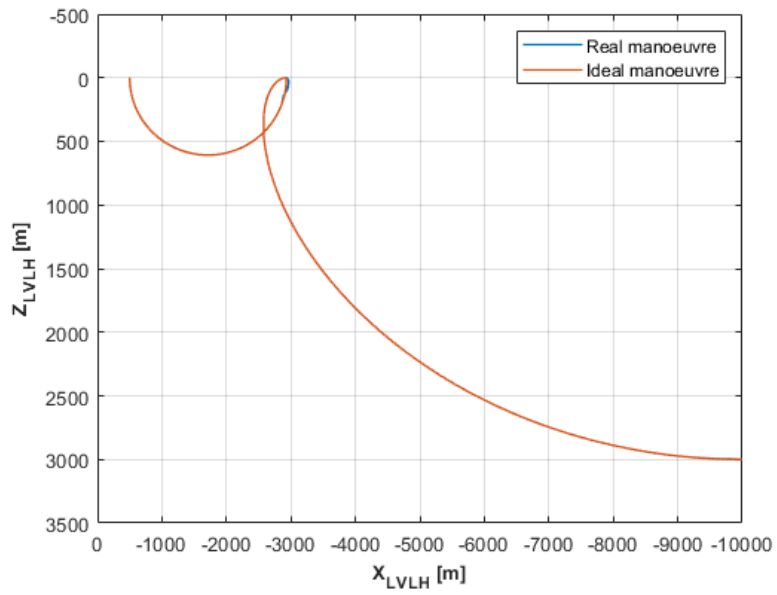


Figure 4.17. Rendezvous manoeuvre

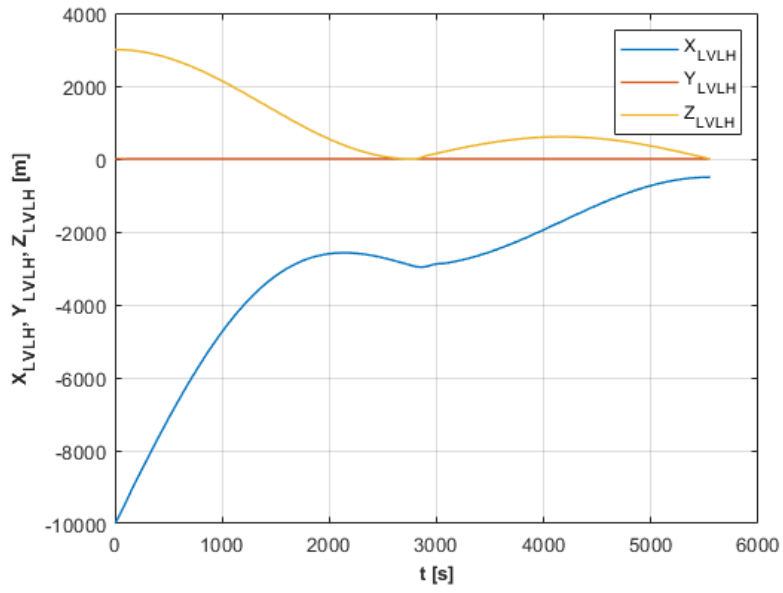


Figure 4.18. Time history of chaser position

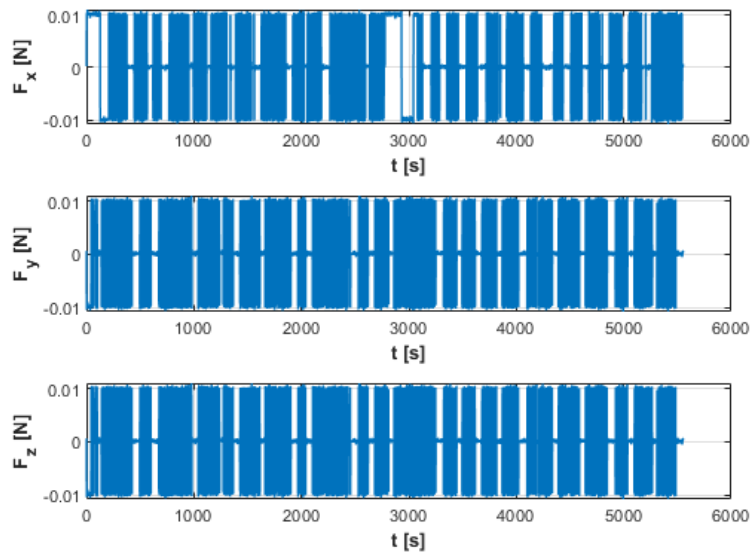


Figure 4.19. Force due to thrusters

Chapter 5

Conclusions

The main objective of this thesis is to design a robust controller for a CMG based testbed. For this purpose, two Sliding Mode techniques are designed. The Sliding Mode control is affected by the chattering effect caused by the presence of unmodeled dynamics in the systems. Since the model used to design the controller can never capture all the system dynamics, it is not possible to obtain a "chattering free" sliding mode control but it is possible to reduce it. The use of High Order Sliding Mode is considered the best option to obtain continuous and "smooth enough" control signals. Two second-order sliding mode controllers are designed, a Super-Twisting (STW) and an Adaptive Continuous Twisting (ACTW), they are two Second Order controller.

The CMG-based spacecraft dynamic equation dynamics is obtained on the base of the Euler's equation that describes the attitude dynamics of rigid bodies. Since the actuators are CMGs, a steering law for solving the singularity problem is introduced.

The simulations are performed in Matlab/Simulink. Then, the external gravity torque due to small misalignment between the center of bearing and the center of gravity of the testbed is included to have a more reliable mathematical model.

Results of the simulation show that the designed controllers are excellent methods to solve the testbed attitude tracking problem. The STW algorithm shows slightly better performance but it has a lower operating range with respect to the ACTW because the last one can change its gains adapting itself to environmental changes and disturbances. The next step will be the implementation of the controllers on the testbed and performing experiments in order to verify the results of simulations. The translation into C++ code (that is the programming language which communicates with the testbed) is partially done, and one experiment was performed, but with a first-order SMC (not included in this thesis).

The last chapter introduce the problem of flexibility during an attitude manoeuvre that interferes with the attitude control. The equation of attitude motion is implemented into the Simulink model to emulate the attitude dynamics. Then, the

position dynamics is added in order to perform a rendezvous manoeuvre composed by an Hohmann transfer and a Radial boost with a H_∞ control law. The purpose is to verify the performances of the same actuators and the same Sliding Mode controller of the testbed on a spacecraft with a similar inertial characteristics. Results show good performances which reveal a fair steady state accuracy and a fast convergence speed. Future directions of research could be focused on the implementation of the final approach. Another development could be the design of a H_∞ taking into account the measurement error and thrust error.

Appendix A

Euler angles

Euler Angles are three independent quantities that define the orientation of a generic reference frame with respect to another reference frame. They were introduced to describe the attitude of a rigid body in the space. The components of a vector relative to the frame $F_1 = (X_1, Y_1, Z_1)$ with unit vectors (i, j, k) are converted into a second frame $F_2 = (X_2, Y_2, Z_2)$ with unit vectors (l, m, n) . There are different ways to express Euler Angles depending on the sequence of rotations, three rotation are needed. The three rotations (with anti-clockwise direction considered positive) are applied to the frame F_2 in order to align it to F_1 . The sequence of rotations is fixed as (ψ, θ, ϕ) as in [5].

- First rot.: positive rotation about Z_2 by ψ , so an intermediate frame is defined $F'_2 = (X'_2, Y'_2, Z'_2)$ with unit vectors (l', m', n') and $Z'_2 \equiv Z_2$;
- second rot.: rotation about Y'_2 by θ . Another intermediate frame is defined $F''_2 = (X''_2, Y''_2, Z''_2)$ with unit vectors (l'', m'', n'') and $Y''_2 \equiv Y'_2$;
- third rot.: rotation about X''_2 by ϕ . Finally, the vector in the desired frame is obtained, $F_1 = (X_1, Y_1, Z_1)$ with unit vectors (i, j, k) , $X''_2 \equiv X_1$.

The matrix formulation is:

$$[\Psi] = \begin{bmatrix} \cos\psi & -\sin\psi & 0 \\ \sin\psi & \cos\psi & 0 \\ 0 & 0 & 1 \end{bmatrix}, \quad [\Theta] = \begin{bmatrix} \cos\theta & 0 & \sin\theta \\ 0 & 1 & 0 \\ -\sin\theta & 0 & \cos\theta \end{bmatrix}, \quad [\Phi] = \begin{bmatrix} 1 & 0 & 0 \\ 0 & \cos\phi & -\sin\phi \\ 0 & \sin\phi & \cos\phi \end{bmatrix} \quad (\text{A.1})$$

If a known vector v_1 is expressed in F_1 , to obtain the same vector in F_2 the following operation is needed:

$$v_2 = [\Psi] \cdot [\Theta] \cdot [\Phi] \cdot v_1 = [L_{21}] \cdot v_1 \quad (\text{A.2})$$

Appendix B

Flexible dynamics

The following definitions and additional information are given in [29].
 M is the generalized $6n$ by $6n$ inertia matrix of cantilevered appendage:

$$M = \begin{bmatrix} m_1 & 0 & 0 & 0 & \dots & 0 \\ 0 & J_1 & 0 & 0 & \dots & 0 \\ 0 & 0 & m_2 & 0 & \dots & 0 \\ 0 & 0 & 0 & J_2 & \dots & 0 \\ \cdot & \cdot & \cdot & \cdot & \dots & \cdot \\ \cdot & \cdot & \cdot & \cdot & \dots & \cdot \\ \cdot & \cdot & \cdot & \cdot & \dots & \cdot \\ 0 & 0 & 0 & 0 & \dots & J_n \end{bmatrix} \quad (\text{B.1})$$

m_i and J_i , $i = 1, \dots, n$, are 3 by 3 mass matrix and inertia matrix respectively of i_{TH} appendages. In this case:

$$m_i = \begin{bmatrix} m_i & 0 & 0 \\ 0 & m_i & 0 \\ 0 & 0 & m_i \end{bmatrix} \quad J_i = \begin{bmatrix} J_x^i & 0 & 0 \\ 0 & J_y^i & 0 \\ 0 & 0 & J_z^i \end{bmatrix} \quad (\text{B.2})$$

J is expressed respect to center of mass and it is diagonal because principal direction of inertia are considered.

The operator \tilde{a} , if $\mathbf{a} = [a_1, a_2, a_3]$ is a generic vector, indicates:

$$\tilde{a} = \begin{bmatrix} 0 & -a_3 & a_2 \\ a_3 & 0 & -a_1 \\ -a_2 & a_1 & 0 \end{bmatrix} \quad (\text{B.3})$$

Moreover, Σ is a boolean operator and if we consider the 3 by 3 identity matrix I and the null matrix 0 , it can be calculated as in:

$$\begin{aligned}\Sigma_{I0} &= [I \ 0 \ I \ 0 \ I \ \dots \ I \ 0]^T \\ \Sigma_{0I} &= [0 \ I \ 0 \ I \ 0 \ \dots \ 0 \ I]^T\end{aligned}\tag{B.4}$$

Appendix C

H_∞

C.1 L_\star norms

The following definitions and additional information are given in [52, 38]. Considering V a finite dimension space, $\forall p \geq 1$, the application $\|\cdot\|_p$ is a norm, defined as:

$$\|v\|_p = (\sum |v_i|^p)^{1/p} \quad (\text{C.1})$$

Let V be a vector a vector space over over \mathbb{C} (or \mathbb{R}) and let $\|\cdot\|$ be a norm defined on V . Then V is a normed space .

The 1-Norm of a function $x(t)$ is given by:

$$\|x(t)\|_1 = \int_0^{+\infty} |x(t)| dt \quad (\text{C.2})$$

The 2-Norm (that introduces the energy norm) is given by,

$$\|x(t)\|_2 = \sqrt{\int_0^{+\infty} |x^*(t)x(t)| dt} = \sqrt{\frac{1}{2\pi} \int_{-\infty}^{+\infty} X^*(j\omega)X(j\omega) d\omega} \quad (\text{C.3})$$

Parseval identity is used to obtain the second equality in equation. In the end, the ∞ -Norm is obtained by:

$$\|x(t)\|_\infty = \sup |x(t)| \quad (\text{C.4})$$

Bibliography

- [1] Giulio Avanzini. *Notes of the Course "Spacecraft Attitude Dynamics and Control"*, Politecnico di Torino. 2008/2009.
- [2] Sarah K. Spurgeon Bijnan Bandyopadhyay S. Janardhanan. *Advances in Sliding Mode Control, Concept, Theory and Implementation*. Springer-Verlag Berlin Heidelberg, 2013.
- [3] Marcello Bonfè. *TECNICHE DI CONTROLLO: SISTEMI NONLINEARI*. URL: http://www.silviosimani.it/Nonlineare_TdC2013.pdf. Università di Ferrara.
- [4] Matthew Brett. *Gimbal lock*. URL: https://matthew-brett.github.io/transforms3d/gimbal_lock.html.
- [5] Elisa Capello. *Notes of the Course "Dinamica e controllo dei veicoli spaziali"*, Politecnico di Torino. 2019/2020.
- [6] J. Chakravorty. "Singularity avoidance in single gimbal CMG using the theory of potential functions". In: *Proceedings of the 10th World Congress on Intelligent Control and Automation*. 2012, pp. 1103–1108.
- [7] *Chapter 9 Robustness and Performance*. URL: http://www.cds.caltech.edu/~murray/courses/cds101/fa04/caltech/am04_ch9-3nov04.pdf.
- [8] M. Ciavola et al. "Comparison of SDA and MPC controllers of a CMG system for the singularity problem". In: *SICE Annual Conference 2019*. 2019.
- [9] Cornelisse, J. W., Schoyer, H. F. R., and Wakker, K. F. *Rocket Propulsion and Spacecraft Dynamics*. Pitman Publishing, London, 1979, Chap. 6.
- [10] H. Curtis. *Orbital Mechanics for Engineering Students*. Elsevier Butterworth-Heinemann, 2005.
- [11] Daiki Higashiyama, Yasuhiro Shoji, Satoshi Satoh, Ichiro Jikuya, Katsuhiko Yamada. "Attitude control for spacecraft using pyramid-type variable-speed control moment gyros". In: *Acta Astronautica* 173.252-265 (2020).
- [12] Robert DiSalle. *Space and Time: Inertial Frames*. URL: <https://plato.stanford.edu/archives/win2020/entries/spacetime-iframe/>. Edward N. Zalta (ed.)

- [13] S. Durga Nair, P. S. Lal Priya, and A. Narayanan. “Quaternion Based Sliding Mode Attitude Controller for a Spacecraft with Control Moment Gyros”. In: *2018 15th International Workshop on Variable Structure Systems (VSS)*. 2018, pp. 245–250. DOI: 10.1109/VSS.2018.8460457.
- [14] Matteo Dentis Elisa Capello. “Precise Attitude Control Techniques: Performance Analysis From Classical to Variable Structure Control”. In: *Advances in Spacecraft Attitude Control 9*, IntechOpen (2020).
- [15] Elisa Capello, Elisabetta Punta, Fabrizio Dabbene, Giorgio Guglieri, Roberto Tempo. “Sliding-Mode Control Strategies for Rendezvous and Docking Maneuvers”. In: *JOURNAL OF GUIDANCE, CONTROL, AND DYNAMICS* 40.6 (June 2017).
- [16] Elbrous M. Jafarov Erkan Abdulhamitbilal. “Design of Sliding Mode Attitude Control for Communication Spacecraft”. In: *Advances in Spacecraft Systems and Orbit Determination 7*, IntechOpen (2012).
- [17] C. Evangelista et al. “Lyapunov-Designed Super-Twisting Sliding Mode Control for Wind Energy Conversion Optimization”. In: *IEEE Transactions on Industrial Electronics* 60.2 (Feb. 2013), pp. 538–545. DOI: 10.1109/TIE.2012.2188256.
- [18] Matteo Facchino. *MPC Design for CMG based Testbed*. Master’s Degree Thesis. 2019/2020.
- [19] Wigbert Fehse. *Automated rendezvous and docking of spacecraft*. Cambridge University Press, 2003.
- [20] Michele Fragnelli. *Attitude e Orbit Control System: come ci si muove nello spazio?* URL: <https://aerospacecue.it/attitude-orbit-control-system-come-muoversi-spazio-satelliti/21951/>.
- [21] S. Di Gennaro. “Output Stabilization of Flexible Spacecraft with Active Vibration Suppression”. In: *IEEE TRANSACTIONS ON AEROSPACE AND ELECTRONIC SYSTEMS* 39.3 (2003).
- [22] Ting Hao and Saburo Matunaga. “New sliding mode control approach for rapid attitude maneuver using control moment gyros”. In: *Journal of Aerospace Engineering* 29.2 (2016), p. 06015001.
- [23] Ting Hao and Saburo Matunaga. “Robust attitude control of nano-satellite using control moment gyros based on higher order sliding modes”. In: *International Journal of Space Science and Engineering* 29 2.3 (2014), pp. 259–275.
- [24] Ting HAO et al. “A Practical Rapid Attitude Maneuver Control System using Control Moment Gyros for Microsatellite TSUBAME”. In: *TRANSACTIONS OF THE JAPAN SOCIETY FOR AERONAUTICAL AND SPACE SCIENCES, AEROSPACE TECHNOLOGY JAPAN* 13 (2015), pp. 37–43.

- [25] Hellerick. *Globe with the Earth surface divided into 1:1,000,000 map sheets of Soviet topographic maps*. URL: https://commons.wikimedia.org/wiki/File:Division_of_the_Earth_into_Gauss-Krueger_zones_-_Globe.svg.
- [26] Raymond H Kraft. “CMG singularity avoidance in attitude control of a flexible spacecraft”. In: *1993 American Control Conference*. IEEE. 1993, pp. 56–58.
- [27] Hyunjae Lee et al. “Singularity avoidance law for CMG using virtual actuator”. In: *IFAC Proceedings Volumes 40.7 (2007)*, pp. 305–310.
- [28] Arie Levant. “Sliding order and sliding accuracy in sliding mode control”. In: *International journal of control* 58.6 (1993), pp. 1247–1263.
- [29] P. W. Likins. *Dynamics and Control of Flexible Space Vehicles*. Jet Propulsion Lab., California Inst. of Tech. Pasadena, CA, United States, 1970.
- [30] M. Mancini and E. Capello. “Adaptive Sliding Mode-based Control System for Flexible Spacecraft”. In: *2021 American Control Conference*. 2021.
- [31] Paolo Gasbarri Marco Sabatini Giovanni B. Palmerini. “A testbed for visual based navigation and control during space rendezvous operations”. In: *Acta Astronautica* 117 (2015).
- [32] F Landis Markley and John L Crassidis. *Fundamentals of spacecraft attitude determination and control*. Vol. 33. Springer, 2014.
- [33] Matteo Facchino, Atsushi Totsuka, Elisa Capello, Satoshi Satoh, Giorgio Guglieri, Katsuhiko Yamada. “Design and Validation of an MPC controller for CMG-based testbed”. In: ().
- [34] Jaime Moreno et al. “Adaptive Continuous Twisting Algorithm”. In: *International Journal of Control* (Nov. 2015), pp. 1–15. DOI: 10.1080/00207179.2015.1116713.
- [35] Autodesk Nastran. *Modal or Natural Frequency Analysis*. URL: <https://knowledge.autodesk.com/support/inventor-nastran/learn-explore/caas/CloudHelp/cloudhelp/2018/ENU/NINCAD-SelfTraining/files/GUID-978425AB-D2FA-491B-8D39-BD1A757F3BBD-htm.html>. (accessed: 22.02.2021).
- [36] Nicoletta Bloise, Elisa Capello, Matteo Dentis, Elisabetta Punta. “Obstacle Avoidance with Potential Field Applied to a Rendezvous Maneuver”. In: *Applied Sciences* 7(10):1042 (2017).
- [37] Carlo Novara. *Notes of the Course "Nonlinear control and aerospace applications"*, Politecnico di Torino. 2020.
- [38] Soheib Fergani Olivier Sename. *Robustness and H control of MIMO systems*. URL: https://hal.univ-grenoble-alpes.fr/hal-01661026/file/IVSS2017_hinf.pdf. (accessed: 22.02.2021).

- [39] Wei Xing Zheng Shihong Ding. “Nonsmooth Attitude Stabilization of a Flexible Spacecraft”. In: *IEEE TRANSACTIONS ON AEROSPACE AND ELECTRONIC SYSTEMS* 50.2 (2014).
- [40] Yuri Shtessel et al. *Sliding mode control and observation*. Springer Science+Business Media, New York, 2014.
- [41] Kanthalakshmi Srinivasan, Deepana Gandhi, and Manikandan Venugopal. “Spacecraft attitude control using control moment gyro reconfiguration”. In: *Studies in Informatics and Control* 23.3 (2014), p. 286.
- [42] Jazmín Zenteno Torres et al. “A Super-Twisting Sliding Mode Control in a Backstepping Setup for Rendezvous with a Passive Target **This work is supported by CONACyT under grant 440473 (CVU 594664), by SIP-IPN under grant 20180865 and by CDA-IPN.” In: *IFAC-PapersOnLine* 52.12 (2019). 21st IFAC Symposium on Automatic Control in Aerospace ACA 2019, pp. 25–30. ISSN: 2405-8963. DOI: <https://doi.org/10.1016/j.ifacol.2019.11.064>. URL: <https://www.sciencedirect.com/science/article/pii/S2405896319309991>.
- [43] Victor Torres-González et al. “Design of continuous twisting algorithm”. In: *Automatica* 80 (2017), pp. 119–126.
- [44] V. I. Utkin. *Variable Structure Control Optimization*. Springer-Verlag, 1992.
- [45] Vadim Utkin, Jurgen Guldner, and Jingxin Shi. “Sliding mode control in electromechanical systems”. In: *Taylor & Francis Ltd* (1999), pp. 115–129.
- [46] Dr. CI Underwood V. Lappas Dr. WH Steyn. “Attitude Control for Small Satellites using Control Moment Gyros”. In: ().
- [47] Bong Wie. “New Singularity Escape/Avoidance Steering Logic for Control Moment Gyro Systems”. In: *Journal of Guidance Control and Dynamics - J GUID CONTROL DYNAM* 28 (Sept. 2005), pp. 948–956. DOI: 10.2514/1.10136.
- [48] Edward Wilson, David Sutter, and Robert Mah. “Motion-based mass-and thruster-property identification for thruster-controlled spacecraft”. In: *Proceedings of the 2005 AIAA Infotech@ Aerospace Conference*. 2005.
- [49] Edward Wilson, David Sutter, and Robert Mah. “Motion-based thruster fault detection and isolation”. In: *Proceedings of the 2005 AIAA Infotech@ Aerospace Conference*. 2005.
- [50] K. D. Young. “Controller Design for Manipulator using Theory of Variable Structure Systems”. In: *IEEE Trans. on System, Man, and Cybernetics* SMC-8. 101-109 (1978).

BIBLIOGRAPHY

- [51] Y. Zhao et al. “Impulsive Super-Twisting Sliding Mode Control for Space Debris Capturing via Tethered Space Net Robot”. In: *IEEE Transactions on Industrial Electronics* 67.8 (2020), pp. 6874–6882. DOI: 10.1109/TIE.2019.2940002.
- [52] Doyle J. Zhou K. and Glover K. *Robust and Optimal Control*. Prentice Hall, 1996.